A Compact Hydraulic Head Auto-Regulating Module (CHARM) for Long-Term Constant Gravity-Driven Flow Microfluidics

by

Fan Xue

B.Eng., Vanderbilt University, 2022

Submitted to the Department of Electrical Engineering and Computer Science
in partial fulfillment of the requirements for the degree of

MASTER OF SCIENCE

at the

MASSACHUSETTS INSTITUTE OF TECHNOLOGY

May 2024

Authored by: Fan Xue
Department of Electrical Engineering and Computer Science
May 17, 2024

Certified by: Joel Voldman
Professor of Electrical Engineering and Computer Science
Thesis Supervisor

Accepted by: Leslie A. Kolodziejski
Professor of Electrical Engineering and Computer Science
Chair, Department Committee on Graduate Students

A Compact Hydraulic Head Auto-Regulating Module (CHARM) for Long-Term Constant Gravity-Driven Flow Microfluidics

by

Fan Xue

Submitted to the Department of Electrical Engineering and Computer Science
on May 17, 2024 in partial fulfillment of the requirements for the degree of

MASTER OF SCIENCE

ABSTRACT

Gravity-driven flow is a simple microfluidic flow initiation and maintenance mechanism that requires no external power sources and low expertise to use. However, the driving forces created by hydraulic head differences gradually decrease during operation, resulting in unwanted decreased flow rates in many microfluidic applications. The existing methods to maintain a constant flow for gravity-driven mechanisms either require additional bulky control equipment, involve complex fabrication or operation, or introduce interfaces that lack robustness. To solve those problems, a compact hydraulic head auto-regulating module (CHARM) was designed and tested in this thesis. The module was able to maintain the liquid level at the microfluidic inlet port within a small fluctuation range without human intervention for a long operation time. The design's compactness and its compatibility with the standard 96 well plates enable high-throughput operations, and the chosen material's bio-compatibility allows the devices' use on cell culture related applications.

Thesis supervisor: Joel Voldman
Title: Professor of Electrical Engineering and Computer Science

Acknowledgments

I would like to thank my thesis supervisor and research advisor, Prof. Joel Voldman, for his invaluable guidance ever since I joined the lab. Not only did he impart his professional expertise, but he also demonstrated himself the greatest qualities that a researcher could have, and helped me overcome my stages of bewilderment, anxiety, and frustration through his understanding and far-sightedness.

I want to thank all current and past members that I have met in the Voldman Group. I cannot image how hard things would be without their friendliness, patience, and support. They made me feel home and treated me as real friends.

I also want to say thank you to those who provide professional trainings for me on the instruments that contributes to this thesis. Steven Nagle trained me on the Stratasys J5 printer used in the final design and helped me brainstormed the design ideas, which enlightened my thoughts; Mark Belanger helped me with milling, lathing, and CNC machining, which were valuable experiences for me, although those techniques were not chosen to be used with the final designs. Many lab members have also provided trainings and support for me on many instruments we used in the lab, such as the microscope and the biosafety cabinet. Their hands-on guidance was priceless for me.

I am also grateful to my past advisors and those people who first guided me into research. I would not have gone this far without their kindness and encouragements.

Lastly, I would like to thank my families and friends who were not directly involved with my research. Even though many of them lived far apart with me, they gave me the warmest support that always lives deep in my heart. Their support has always been my emotional backup, and no words can convey how grateful I am to them.

Contents

List of Figures

Chapter 1

Introduction

1.1 Flow Mechanisms for Microfluidic Designs

1.1.1 Microfluidics Overview

Microfluidics pertains to the science and technology that enables precise fluid manipulation in channels with dimensions of tens of micrometers. [1], [2] Some unique properties emerge or are amplified at the micrometer scale, including laminar flow dominated by viscous forces, capillary effect, rapid reaction rate, and significant surface effects. [2], [3] By utilizing those properties and possessing the capacity to achieve rapid, sensitive, low-cost, high-throughput analysis and synthesis [2], [4] microfluidics have shown great capabilities and potentials in numerous applications such as disease diagnosis, cell analysis, drug delivery, and nanomaterial synthesis. [4]–[6] Particularly, for cell culture related applications, microfluidic chips enable media perfusion, which provides a shear stress important for the growth of certain types of cells, such as endothelial cells[7], [8], and continuously provide nutrients and remove metabolic wastes for a more stable culture environment.

While the channel geometries or working region functions of the microfluidic chips vary greatly between different designs, the flow regions are typically interfaced with other systems through one or more input and output ports, where a pressure difference is generated in

between by pumps or other mechanisms to provide a driving force to create flow within the chip. The flow mechanisms, depending on the types of driving forces, can generally be categorized into active pumping mechanisms and passive pumpless mechanisms, which are further explained in the next two sections.

1.1.2 Active Pumping Mechanisms for Microfluidics

Active pumping mechanisms for microfluidics involve driving fluid through an external power source/field or actuators. [9] Some common active pumps (Fig. 1.1) for microfluidics include syringe pumps [10]–[12], peristaltic pumps [13], [14], piezoelectric pumps [15]–[17], and magnetic pumps [18]–[20].

While active pumping methods generally have precise controls on the port pressures or flow patterns, they typically require external off-chip controllers, which limits their use for high-throughput applications where tens of pumps are needed in parallel. Also, for cell culture related applications, wiring the power cords into the incubator can negatively affect the sterility and temperature or humidity control of the incubator. Moreover, interfacing with external controls can easily introduce bubbles to fluidic channels, and dead volumes associated with tubing connections lead to waste of expensive reagents. Some efforts have been done to alleviate those issues by integrating the pumps onto chips [21]–[24], but those pumps still require complex manufacturing procedures and external power sources.

1.1.3 Passive Pumpless Flow Mechanisms for Microfluidics

On the other hand, passive flow techniques do not require external power source or actuators. Some examples of passive flow are shown in Fig. 1.2. Devices configured for passive flow techniques take advantage of the potential energy of the fluid itself, including osmotic potential energy for osmosis-driven flow [26]–[28], surface energy for surface tension-driven flow [29]–[31] and capillary-driven flow [32]–[35], and gravitational potential energy for gravity-driven flow [36]–[48]. Those techniques are self-operational without external controls, and are gener-

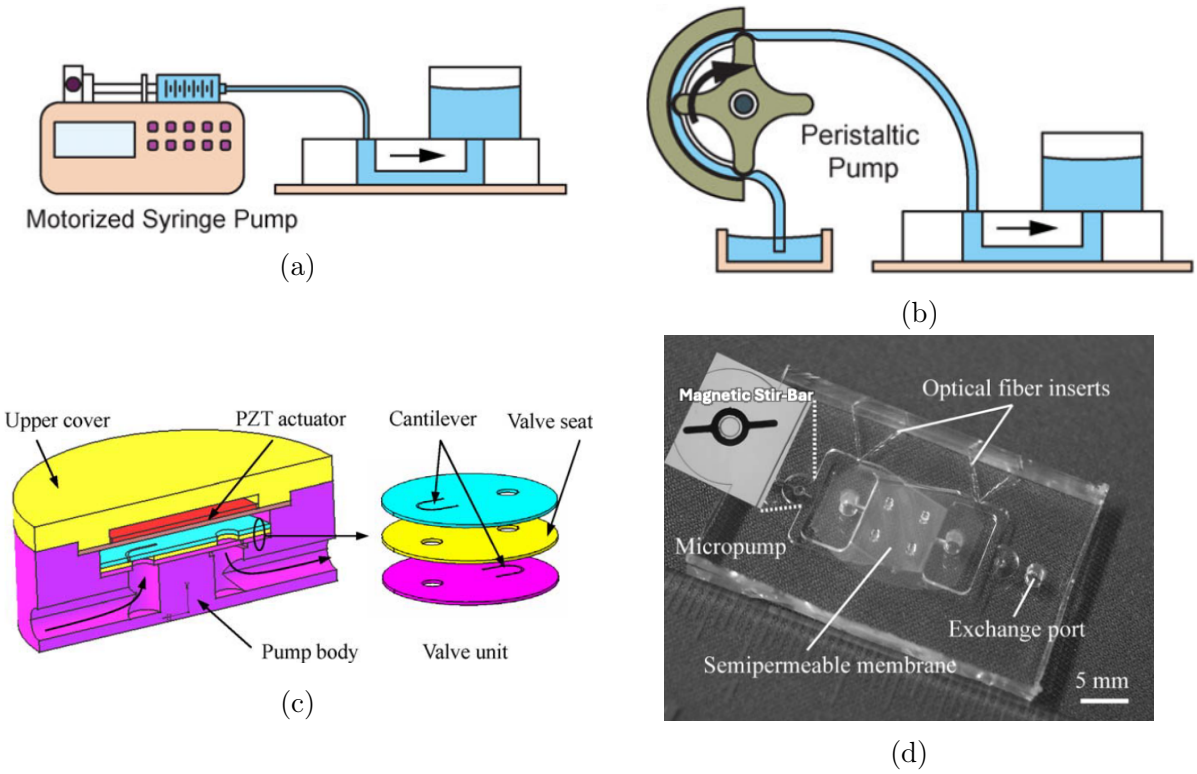

Figure 1.1: Examples of active pumping mechanisms for microfluidics. (a) Syringe pump. Syringes are attached to a motor that pushes the plungers at a set speed. Reproduced from [25] with permission. (b) Peristaltic pump. Liquid is pinched forward through the tubing by the rotor. Reproduced from [25] with permission. (c) Piezoelectric pump. The piezoelectric actuator's vibration pushes the two valves to open and close consecutively, which propels liquid forward. Reproduced from [17] with permission. (d) Magnetic pump. A magnetic stir-bar is used to push liquid through the microfluidic design. Adapted from [19] with permission. Other configurations not shown here using magnetic or electromagnetic forces also exit.

ally more compact and less bubble-prone than the active pumping mechanisms. The elimination of bulky power sources allows easy integration of those flow mechanisms on chip, which reduces the device footprint and decrease the difficulty of fluid handling. Because of those advantages, passive flow techniques are becoming more and more popular for lab-on-chip or point-of-care microfluidic systems. [9]

However, many of the discussed passive techniques have their own limitations. Osmosis-driven flow requires a complex setup involving a proper semi-permeable membrane [9], and do not have flexibility in fluid concentrations. Surface tension-driven flow and capillary-

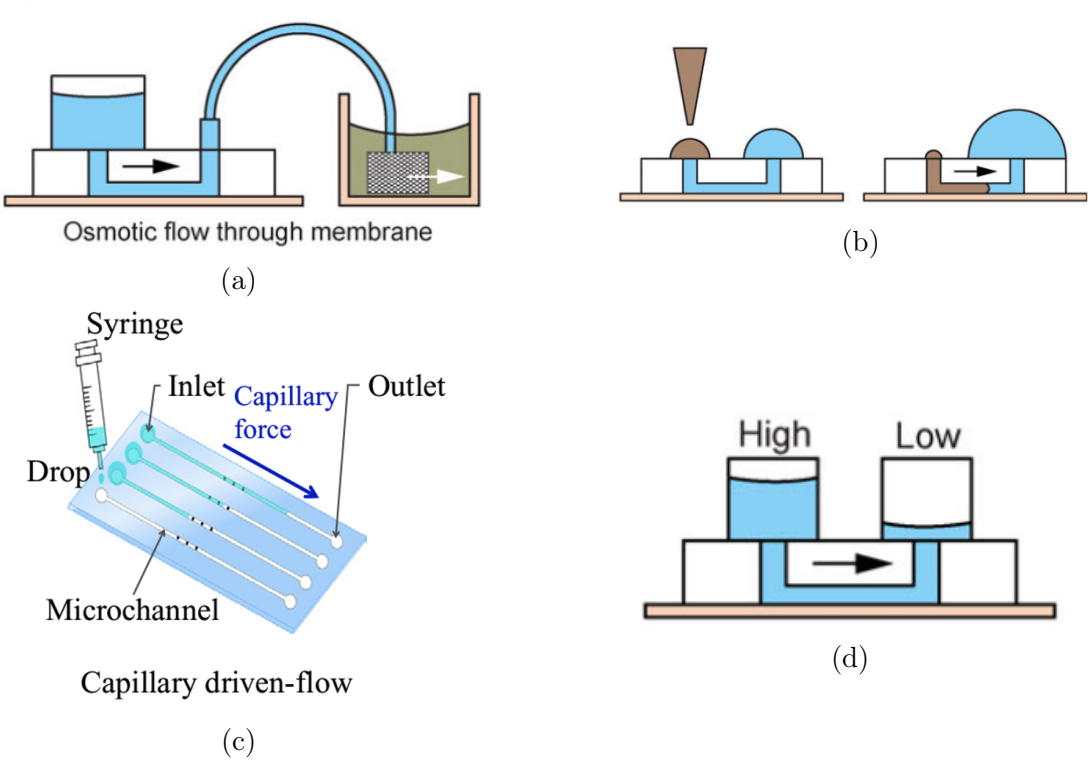

Figure 1.2: Examples of passive pumpless flow mechanisms for microfluidics. (a) Osmosis-driven flow. The osmotic difference of solutions between the semi-permeable membrane drives solvent to flow towards the high-concentration region. Reproduced from [25] with permission. (b) Surface tension-driven flow. The smaller droplet on the inlet holds a larger surface pressure than the bigger droplet on the outlet, which drives the flow through the channel. Reproduced from [25] with permission. (c) Capillary-driven flow. The hydrophilic channel creates an adhesion force that allows the liquid to fill the entire channel without external pressures. Reproduced from [35] with permission. (d) Gravity-driven flow. The hydrostatic pressure difference generated by the height difference between the liquid columns from the inlet and outlet drives the liquid flow. Reproduced from [25] with permission.
.

driven flow depend on the device material and fluid properties, which limits the device's adaptability to new systems and flexibility to generate self-regulated flows.

On the other hand, gravity-driven flow transcend in its simplicity in both fabrication and operation, because the device needs no extra components, and the driving force can be easily created by altering the relative fluid height between the flow inlet and outlet. Along with its compactness and low expertise barrier, gravity-driven flow has become a popular choice for microfluidic designs that need simple flow profiles.

1.2 Gravity-Driven Flow for Microfluidics

Gravity-driven flow takes advantage of the hydrostatic pressure difference generated by liquid with different heights (hydraulic heads). Hydrostatic pressure, $P_{hydrostatic}$, refers to the pressure exerted by a fluid at equilibrium at any particular point of time due to the force of gravity, and is given by the equation:

$$P_{hydrostatic} = \rho g h \tag{1.1}$$

where ρ is the fluid density, g is the standard gravity, and h is the fluid height from an arbitrary reference point. The absolute pressure at the bottom of a fluid, $P_{absolute}$, is given by the sum of the hydrostatic pressure and the gas pressure above the liquid:

$$P_{absolute} = P_{gas} + \rho g h \tag{1.2}$$

If the fluid is open to the air, the gas pressure is equal to the atmospheric pressure, P_{atm}, so the equation becomes:

$$P_{absolute} = P_{atm} + \rho g h \tag{1.3}$$

Therefore, the absolute pressure difference (ΔP) between the inlet and outlet of a microfluidic chip can be expressed as:

$$\Delta P = (P_{atm} + \rho g h_{in}) - (P_{atm} + \rho g h_{out}) = \rho g \Delta h \tag{1.4}$$

where Δh is the hydraulic head difference between the inlet and outlet, assuming Δh is small enough that P_{atm} stays the same at both locations. This absolute pressure difference is what drives the flow in the microfluidic chip. Since ρ and g are usually constants for incompressible fluids like water, people generally alter Δh to alter the driving force.

Besides having an inlet container that has a higher fluid level than the outlet con-

tainer [36], [37], [48], there are also other ways to generate Δh, including tilting the device [38], [39], or turning a horizontal chip into a vertical direction [40]. However, in traditional gravity-driven flow, the fluid levels change as time passes by, so the pressure varies, leading to variations in flow rate, which is a limitation in many microfluidic systems that require a constant flow. For example, a constant, continuous flow rate is usually needed in cell culture applications where a steady media perfusion is needed to maintain a stable microenvironment for cell growth [49], [50], in laminar stream generation applications where the generated streams need to be kept at a specific width [51], [52], and in droplet microfluidics where liquids need to be infused at a constant rate to ensure uniformity of the emulsions [3], [53].

Efforts have been made to maintain a relatively constant flow rate for gravity-driven flow devices [36], [41]–[45], [53], [54]. Fig. 1.3a shows a gravity-driven flow system with a capacitive fluid level sensor on the outside of the container to maintain desired fluid heights in a small reservoir [43]. Komeya et al. developed a system (Fig. 1.3b) where there was a wide inlet reservoir and a high-resistance circuit to decrease the rate of change of the hydraulic head difference [36]. Researchers have also tried to keep the liquid heights constant by using horizontal inlet and outlet reservoirs [44], [45] as shown in Fig. 1.3c. Gao et al. developed a system (Fig. 1.3d) where the inlet container is continuously being refilled and the any liquid over a certain height is collected by an overfill container. [53] Limjanthong et al. put gravity-driven flow devices on top of a slowly tilting plate that balances the liquid height decrease over time (Fig. 1.3e). [54]

There are also many other systems that uses similar approaches to keep the pressure source constant in gravity-driven flow [41], [42], [55]. However, most of the existing approaches either introduce an additional bulky controller, increase fabrication or operation complexity, or create interfaces that decrease device robustness. These features make them not suitable for use with high-throughput, robust applications.

In 2018, Wang et al. developed an autofill device (Fig. 1.4) that used two straws and a

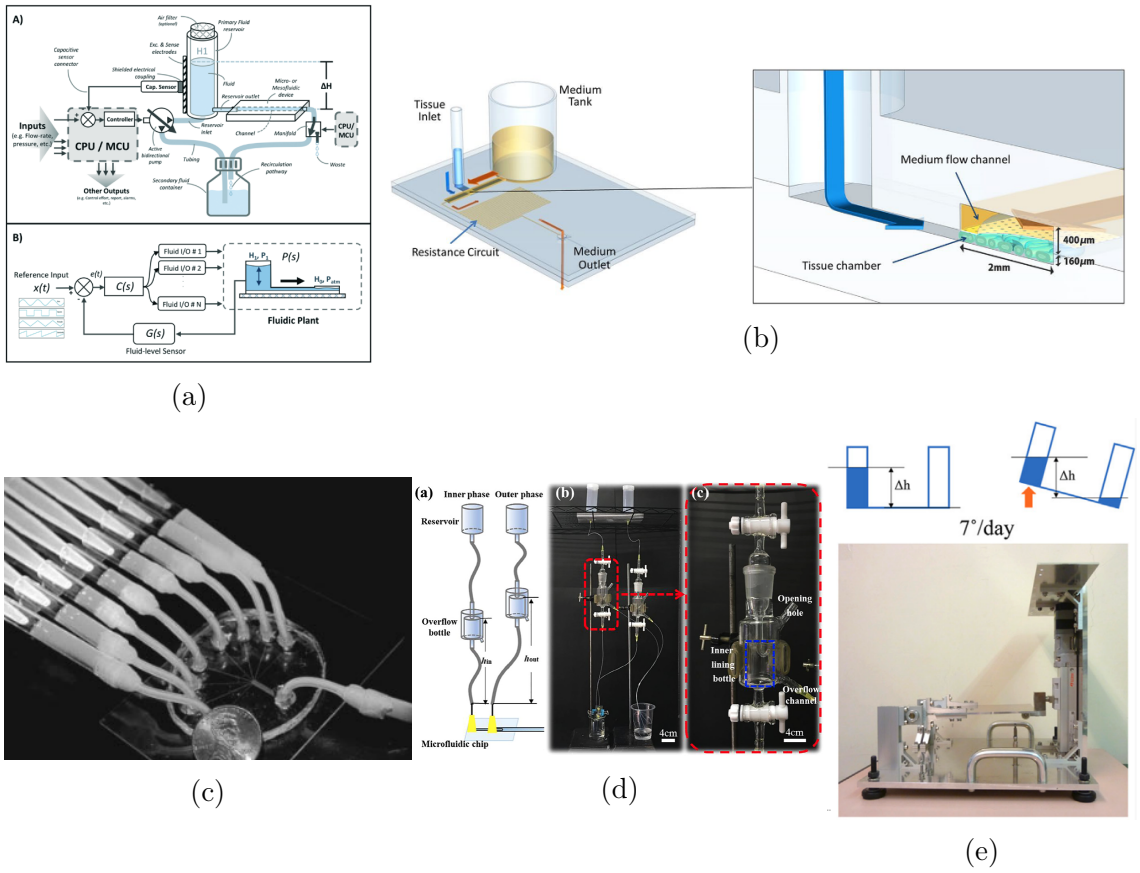

Figure 1.3: Existing gravity-driven flow approaches to make the flow constant. (a) Capacitive sensing feedback control with additional pumps and processors. Reproduced from [43] with permission from the Royal Society of Chemistry. (b) Wide reservoir and high resistance circuit decrease the rate of liquid height change. Reproduced from [36] with permission. (c) Horizontal reservoirs keep the inlets and outlet at constant heights. Adapted from [45] with permission. (d) Overflow channel collects any excess liquid filled beyond a certain height at the inlet. Reproduced from [53] with permission. (e) Slowly tilting plate balances the liquid height decrease. Adapted from [54] with permission.

liquid barrier to control the filling and refilling of fluid in the reservoir. [56] A more detailed explanation of the working principle is included in the next section. This system can maintain a constant flow rate for a prolonged period of time (>14 days). However, the device is bulky and hard to be used on high-thoughput systems, although the critical components in the system (straws and membrane) are simple and can be made compact. Therefore, in this thesis, we aim to use the principle of Wang's autofill device to develop a more compact system to control the fluid height in containers as small as a well in a 96-well microtiter

plate.

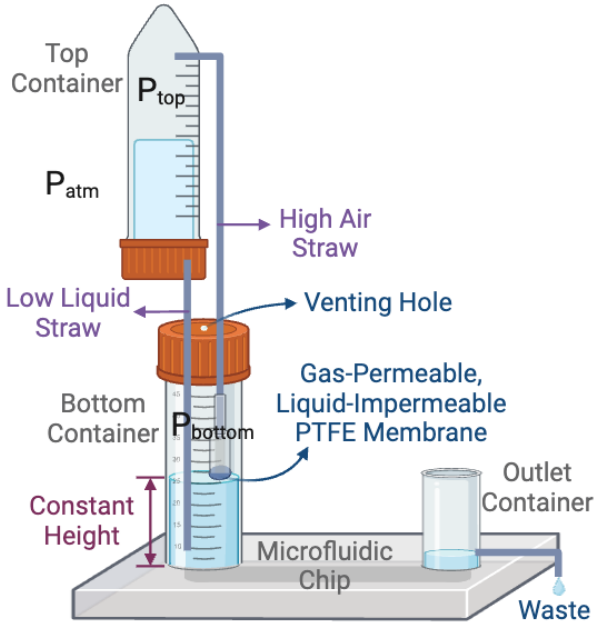

Figure 1.4: Setup of the autofill device from Wang [56]. Note that the "Venting Hole" is not in Wang's original publication, but is needed for the system to function properly. Created with BioRender.com.

1.2.1 General principle of the autofill device [56]

The autofill device developed by Wang et al. [56] (Fig. 1.4) is composed of a top container (which they called the medium storage container) connected with two straws (tubings), which when interfaced with a bottom container (inlet medium reservoir), maintains the fluid level at the bottom container constant. The bottom end of the high straw is connected to a gas-permeable, liquid-impermeable polytetrafluoroethylene (PTFE) membrane. As the liquid in the top container is being filled into the bottom container through the low straw, air goes up through the membrane and the high straw to the top container to balance the pressure drop within. When the liquid level in the bottom container reaches the membrane at the lower end of the high straw, the air pathway is blocked, and the pressure drop in the top container will prevent liquid from further going down through the low straw. Therefore, the liquid stops at the membrane level after the initial fill. The height difference between the liquid

levels in the bottom container and outlet container (outlet medium reservoir) generates a pressure difference that drives the liquid flow in the microfluidic chip. As the liquid level drops below the membrane level, the air pathway in the high straw opens again, allowing pressure in the top container to be balanced, and the liquid to refill to the membrane level. Therefore, a constant liquid level is maintained at the membrane level until the fluid runs out. As any excess liquid in the outlet container will be diverted out as waste, the liquid level in the outlet container is maintained constant too. Therefore, the liquid height difference is kept constant throughout the process, which results in constant pressure perfusion in the microfluidic chip.

It should be noted that the venting hole shown in Fig. 1.4 is not in Wang's original publication. However, the bottom container needs to be open to the air for the system to work properly. If the bottom container is sealed, the gas pressure in both the top (P_{top}) and bottom container (P_{bottom}) will gradually decrease as perfusion drains out liquid from the two containers. In this situation, the absolute pressure difference driving the flow, ΔP, in equation 1.4 becomes

$$\Delta P = (P_{bottom} + \rho g h_{in}) - (P_{atm} + \rho g h_{out}) = \rho g \Delta h + P_{bottom} - P_{atm} \tag{1.5}$$

Although Δh stays the same because the liquid height is still maintained at the membrane level, the absolute pressure difference (ΔP) is decreasing as P_{bottom} is decreasing, resulting in a decreasing driving force. Therefore, P_{bottom} needs to be kept equal to P_{atm}, and a venting hold is added for a more rigorous illustration.

1.3 Proposed System

Although Wang's design solves the inconstant flow problem for gravity-driven flow, the excessive tubing and containers and their integration make it difficult to scale the system up and to be used with smaller containers. We proposed a compact hydraulic head auto

regulating module (CHARM) that (Fig. 1.5) is designed to keep the original function of the autofill device while minimize the device footprint, so that it can be used with the standard 96 well plates and multiple parallelized experiments can be run to achieve a higher throughput.

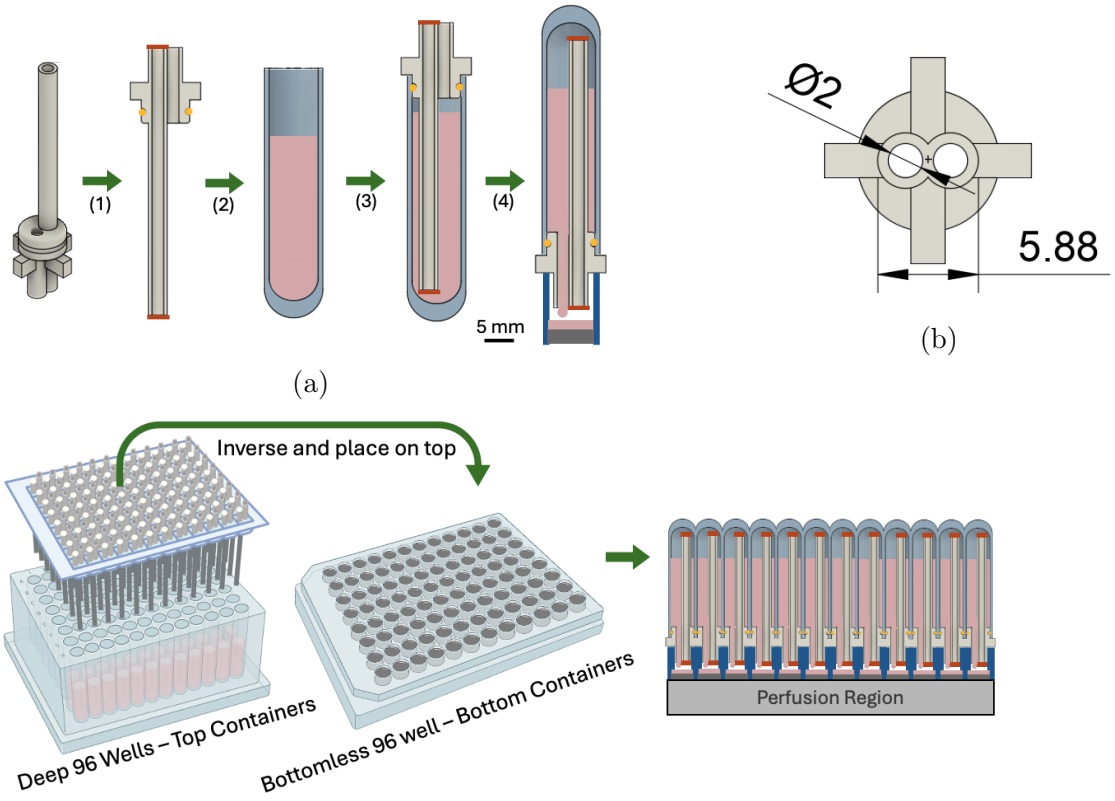

Figure 1.5: CHARM setup. (a) Single system view. (1) Membranes (orange) and O-ring (yellow) are integrated with the device body. (2) The top container is filled with liquid to be perfused. (3) The device body is inserted into the top container. The O-ring helps to seal the edge around the device body. (4) The device is flipped and placed on top of the bottom container connected with the perfusion region (gray). Liquid will be filled to and maintained at the bottom membrane. (b) Bottom view of the single device body. The dimensions are shown in mm. (c) Full system view. The connected device bodies with membranes and o-rings (not shown) are inserted into the 96 deep well plate containing liquid to be perfused. The entire device is then flipped and placed on top of a 96 bottomless well plate connected to the perfusion region to form and maintain a constant liquid level within the bottomless well. Created with BioRender.com.

As shown in Fig. 1.5c, the full system of CHARM uses a round-bottom deep 96-well plate as the top container and a bottomless 96-well plate as the bottom container that is open to the air during operation. The single system view (Fig. 1.5a) shows how each well in the full

system looks like during assembly. After filling the deep well plate with the desired liquid, the device body composed of straws with integrated membranes and O-rings can be inserted into the top container to seal it. After inverting the deep wells into the operating orientation and positioning them on top of the bottomless wells, liquid starts to fill the bottomless wells that are connected to the perfusion regions, and a constant level can be maintained within the bottomless well.

Some modifications are made to the structure of the autofill device for working with the smaller scale:

- The air straw is moved to the inside of the top container for compactness.
- The liquid straw and the air straw share the same wall (Fig. 1.5b) for maximal space usage since the 96 wells have very small diameters ($\sim$ 6.4 mm ID).
- The liquid straw is kept at the same level as the air straw at the bottom end, so that membrane integration will be easier on the bottom end.
- Another membrane is added to the top end of the air straw to prevent liquid from getting into the air straw and interfere with the system's function.
- An O-ring groove is added around the device body so that the top containers can be fully sealed.

Although the device body is designed to be used with 96 well plates, it can be used with other configurations as well. Depending on the experiment, single devices 1.6a, devices in-a-row 1.6b, multiple-fluid perfusion 1.6c or other configurations can be achieved with slight modifications on the system.

In this work, the single device design was used for experiments, and we will demonstrate that our CHARM maintains a constant fluid level in the bottom containers as a constant passive pressure source for flow initiation and maintenance. By automatically filling the reservoir until the fluid level reaches a predetermined height, our device offers self-operability

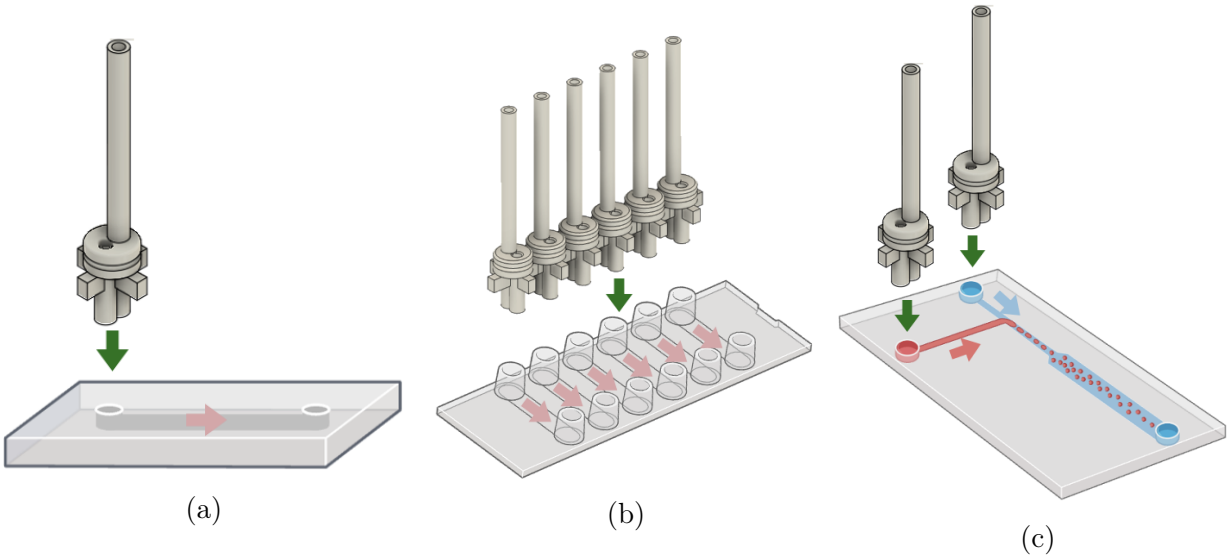

(a) (b) (c)

Figure 1.6: More configurations of CHARM. (a) Single device configuration. Suitable for initial testings. Created with BioRender.com. (b) Multiple devices in a row. Suitable for small scale parallelized testings. Created with BioRender.com. (c) Multiple fluid manipulation on the same microfluidic chip. Created with BioRender.com.

over extended periods, ensuring constant fluid levels without human intervention. Without the use of external tubing, our device is less bubble-prone, and more robust than the other tubing-required systems. Fabricated with low-cytotoxicity materials, CHARM can be used with cell culture applications that require medium perfusion. Its compatibility with 96-well plates and other compact, multiple-open-access devices enables seamless integration with high-throughput applications.

1.4 Thesis Overview

To investigate and demonstrate the proposed system, the main objectives of the thesis are listed as follows:

1. To analyze the working principles of the design and quantify important processes during operation. (Chapter 2)

2. To choose appropriate materials and fabrication methods for the design and demon-

strate its compatibility with cell culture applications through cytotoxicity experiments. (Chapter 3)

3. To validate the working principles and the calculated operational features of CHARM experimentally. (Chapter 3)

Finally, contributions and future work with this device were presented in Chapter 4.

Chapter 2

Theoretical Analysis

2.1 Introduction

Although the working principle of CHARM has already been discussed in Sections 1.2.1 and 1.3, it is still important to analyze the quantitative effects of device parameters to inform design choices and to characterize the limitations of the applicable working conditions.

Firstly, our device filling rate needs to be larger than the perfusion rate in the microfluidic chips for the liquid level and driving force to maintain. Therefore, it is important to characterize the filling rate of the design to determine the target microfluidic perfusion rate range. Secondly, when the liquid reaches the desired level and the air pathway is blocked, it is beneficial to know the exact mechanism that stops the liquid filling. Thirdly, since the bottom container is open to the air, evaporation can play a role if we desire operation over a long range of time. In fact, the device filling rate needs to be larger than the sum of the microfluidic chip perfusion rate and the evaporation rate in the bottom container. Also, the evaporation of the top container liquid also needs to be considered since evaporation can produce changes in the gas pressure in the top container.

In this chapter, we quantified the filling and refilling rate of CHARM (Section 2.2), analyzed the mechanism that stops liquid filling (Section 2.3), and evaluated the effects of

evaporation on the functioning of the device (Section 2.4).

2.2 Filling and Refilling Rate

When the device is initially filling into the bottom container, the system can be considered as liquid draining out from a container (top container) through a cylinder attached vertically to the bottom of the container (Fig. 2.1a). The gas in the top container is connected to the atmosphere by a channel with membranes of resistance (R_m) attached on both ends.

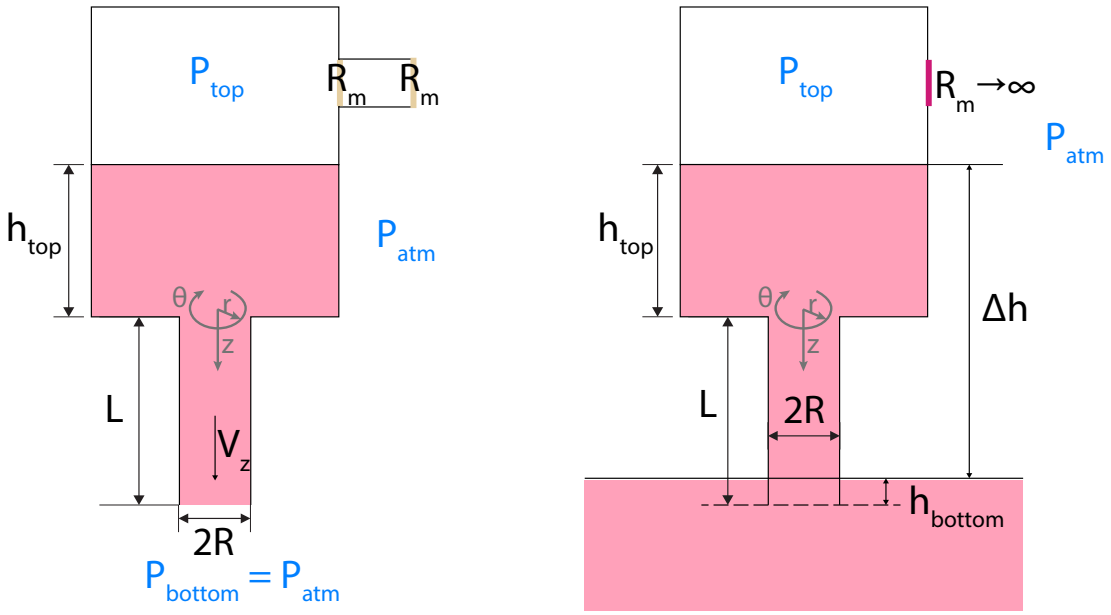

Figure 2.1: Theoretical equivalents of CHARM during operation. (a) Model used during filling/refilling. (b) Model used when membranes are blocked. The overfilling height (h_{bottom}) was exaggerated for better visualization.

Assuming the fluid is continuous and incompressible, the following two equations [57] apply to the liquid in the cylinder:

1. Continuity Equation in cylindrical coordinates:

$$\frac{1}{r}\frac{\partial}{\partial r}(rv_r) + \frac{1}{r}\frac{\partial}{\partial \theta}(v_\theta) + \frac{\partial}{\partial z}(v_z) = 0 \tag{2.1}$$

where v_r, v_θ, and v_z are the fluid velocities in the radial, circumferential, and longitudinal directions, respectively, and r is the distance of the point of interest to the central axis of the cylinder.

2. Navier-Stokes equation for the longitudinal (z) component in cylindrical coordinates:

$$\rho(\frac{\partial v_z}{\partial t}+v_r\frac{\partial v_z}{\partial r}+\frac{v_\theta}{r}\frac{\partial v_z}{\partial \theta}+v_z\frac{\partial v_z}{\partial z})=-\frac{\partial P}{\partial z}+\rho g_z+\mu(\frac{1}{r}\frac{\partial}{\partial r}(r\frac{\partial v_z}{\partial r})+\frac{1}{r^2}\frac{\partial^2 v_z}{\partial \theta^2}+\frac{\partial^2 v_z}{\partial z^2}) \quad (2.2)$$

where ρ is the fluid density, g_z is the gravitational acceleration in the z direction, and μ is the fluid viscosity.

Assuming steady flow ($\partial v_z/\partial t = 0$), no flow in the radial or circumferential directions ($v_r = 0$ and $v_\theta = 0$), and axisymmetric flow ($\partial v_z/\partial v_\theta = 0$), Eq. 2.1 becomes

$$\frac{\mathrm{d}v_z}{\mathrm{d}z}=0 \quad (2.3)$$

which implies that the flow is fully developed, and Eq. 2.2 can then be simplified to

$$\frac{\partial P}{\partial z}=\mu\frac{1}{r}\frac{\partial}{\partial r}(r\frac{\partial v_z}{\partial r})+\rho g_z \quad (2.4)$$

Assuming uniform pressure drop across the cylinder of length L, the pressure gradient can be expressed as

$$\frac{\partial P}{\partial z}=-\frac{\Delta P}{L} \quad (2.5)$$

where ΔP, expressed in the following equation, is the pressure difference between the top end and bottom end of the cylinder without considering the gravity of the fluid in the cylinder

$$\Delta P=\rho g h_{top}+P_{top}-P_{bottom} \quad (2.6)$$

and h_{top} is the height of the top container liquid level measured from the bottom of the top container (Fig. 2.1a).

It can be inferred from device configuration that $P_{bottom} = P_{atm}$, and assuming the membrane has negligible resistance to air and P_{top} is instantaneously balanced to P_{atm} when the membrane is not blocked, the above equation becomes

$$\Delta P = \rho g h_{top} \tag{2.7}$$

Therefore, Eq. 2.5 becomes

$$\frac{\partial P}{\partial z} = -\rho g \frac{h_{top}}{L} \tag{2.8}$$

Assume the cylinder is perfectly vertical, then g_z in Eq. 2.4 is equal to the standard gravity, g (= 9.81 N/kg). Plugging this relation and Eq. 2.8 into Eq. 2.4 gives

$$-\rho g \frac{h_{top}}{L} = \mu \frac{1}{r} \frac{\partial}{\partial r} (r \frac{\partial v_z}{\partial r}) + \rho g \tag{2.9}$$

Two boundary conditions below apply for the system:

1. Finite flow in the center of the cylinder: V_z is finite at $r = 0$, and

2. No slip at wall: $v_z = 0$ at $r = R$, where R is the radius of the cylinder.

Integrating Eq. 2.9 with the boundary conditions above results in the following flow profile:

$$v_z(r) = (\frac{\rho g(h_{top}/L + 1)}{4\mu})(R^2 - r^2) \tag{2.10}$$

The volumetric flow rate down the cylinder (Q) can then be calculated as the integration of the above equation over the cross sectional area of the cylinder:

$$Q = \frac{\pi R^4}{8\mu L} \rho g (h_{top} + L) \tag{2.11}$$

This equation is analogous to the Hagen-Poiseuille equation [58]:

$$Q = \frac{\pi R^4}{8\mu L}\Delta P \tag{2.12}$$

where the pressure term, ΔP, is replaced by the pressure difference between the water level in the top container and the bottom end of the cylinder, $\rho g(h_{top} + L)$. In fact, the discussed derivation process is similar to that for the Hagen-Poiseuille equation, except that an extra gravity term, g_z, remains in the Navier-Stokes equation. Lemons et al. [59] reaches the same conclusion in a similar system as well, although the derivation process is a little different.

If air cannot pass through the membrane freely ($R_m > 0$), then a pressure drop will build up across the membrane, causing the pressure above the water level in the top container to decrease, resulting in a lower filling speed.

Assume the pressure drop across the membrane (ΔP_{air}) changes linearly with the air flow across the membrane (Q_{air}), then $R_m = \Delta P_{air}/Q_{air}$ is a constant and can be added to Eq. 2.11 as an extra resistance component:

$$Q = \rho g(h_{top} + L)/(\frac{8\mu L}{\pi R^4} + 2 * R_m) \tag{2.13}$$

with the factor of 2 indicating the presence of 2 membranes. This resistance can be measured for the specific membrane used.

An estimate of the numerical value for Q is calculated to be 15.7 mL/s using the approximated parameters for our system ($\mu = \mu_{water} = 10^{-3}$ Pa $\cdot$ s, $\rho = 1000$ kg/m^3, $R = 1$ mm, $L = 13$ mm, $h_{top} = 40$ mm, $R_m = 0$). This value is much larger than the perfusion rate required by most microfluidic chips.

After the initial filling cycle, the liquid level in the bottom container drops below the membrane level again and the subsequent refilling cycles are similar to the initial filling cycle. However, h_{top} becomes smaller as the cycle number increases, so the refilling rate is expected to be smaller in each subsequent refilling. Also, the membrane can be partially

blocked by liquid retaining on the membrane after the initial cycle. This is equivalent to having a higher membrane resistance, and will result in a slower refilling rate. Therefore, it is important in the design that the geometries allow a flow rate much greater than the perfusion rate in the microfluidic chip to compensate the flow rate decrease over time.

2.3 The Blocked Air Pathway Stops Liquid Filling

After the membrane is blocked, R_m goes to infinity, and the drop of pressure in the top container (P_{top}) can no longer be balanced by the atmospheric pressure (P_{atm}), so P_{top} decreases until the pressure driving the filling reaches zero. The equilibrium happens when

$$(P_{top} + \rho g(h_{top} + L)) - (P_{atm} + \rho g h_{bottom}) = 0 \tag{2.14}$$

where h_{bottom} is the overfilling height in the bottom container (Fig. 2.1b). At this point, Q in Eq. 2.13 reaches zero with $R_m \to \infty$.

Let Δh be the relative height difference between the fluid level from the top and bottom containers, then

$$\Delta h = h_{top} + L - h_{bottom} \tag{2.15}$$

So Eq. 2.14 becomes

$$P_{top} = P_{atm} - \rho g \Delta h \tag{2.16}$$

The ideal gas law states that

$$PV = nR_{const}T \tag{2.17}$$

where P, V, and T are the gas pressure, gas volume, and gas temperature, respectively. $R_{const} = 8.314 J/mol \cdot K$ is the ideal gas constant.

Let V_{orig} be the original gas volume in the top container and the air straw combined, and V_{new} be the new gas volume at equilibrium. Since the amount of gas (n_{gas}) stays constant

in the top container and air straw after the bottom membrane is blocked, and we assume no change in T,

$$P_{atm}V_{orig} = P_{top}V_{new} = n_{gas}R_{const}T = \text{constant} \tag{2.18}$$

The following relationship between V_{orig} and V_{new} can be derived from Eq. 2.16 and Eq. 2.18:

$$V_{new} = \frac{P_{atm}}{P_{atm} - \rho g \Delta h} V_{orig} \tag{2.19}$$

Therefore,

$$\Delta V = V_{new} - V_{orig} = \frac{\rho g \Delta h}{P_{atm} - \rho g \Delta h} V_{orig} \tag{2.20}$$

Depending on the device height used and the current working condition, Δh varies, but is within 5 cm for the proposed system. Therefore, substituting Δh with $\Delta h_{max} = 0.05$ m, and plugging in $P_{atm} = 101325$ Pa, $g = 9.81$ N/kg, and $\rho = 1000$ kg/m^3 to Eq. 2.20 gives

$$\Delta V_{max} = \frac{490.5}{101325 - 490.5} V_{orig} = 0.00486 V_{orig} \tag{2.21}$$

This indicates that the gas volume increase in the top container and the air straw is less than 1%. If the bottom container and the top container has the same diameter, the overfill height in the bottom container will be less than 1% of the height of the air column in the top container, which is equal to V_{orig}/A_{top}. This results in less than 1 mm change in the overfill height.

2.4 Evaporation

Before delving into the calculations for evaporation in the system, it is important to understand some basic terms related to humidity level or evaporation. Below is a list of terms and equations that are important to the calculation of evaporation for the system:

- Relative humidity (RH) is a measurement of the percentage of partial pressure of water

vapor in air (P_w) relative to the saturation water temperature (P_{ws}) at the current temperature [60]:

$$RH = \frac{P_w}{P_w s} * 100\% \tag{2.22}$$

- The saturation water pressure is dependent on the air temperature only, and can be approximated by the Buck Equation [61]:

$$P_{ws} = 611.21 * \exp\left(18.678 - \frac{T_C}{234.5}\right)\left(\frac{T_C}{257.14 + T_C}\right) \tag{2.23}$$

  where T_C is the air temperature in °C.

- The net evaporation rate, defined as the gross evaporation rate minus the condensation rate, is larger than zero when RH is smaller than 100%. At 100% RH, P_w is equal to P_{ws}, and net evaporation ceases.

- Specific humidity (SH) is defined as the ratio of the mass of water vapor (m_w) to the total mass of water vapor (m_w) and dry air (m_{air}) [60]:

$$SH = \frac{m_w}{m_w + m_{air}} * 100\% \tag{2.24}$$

  In regular air where the average molecular weight of gases is 28.964 g/mol, it can be determined from Eq. 2.24 and the ideal gas law (Eq. 2.17) that

$$SH = 0.622 * \frac{P_w/P_{total}}{1 - P_w/P_{total} + 0.622 * P_w/P_{total}} * 100\% \tag{2.25}$$

- Air density (AD) equals to the mass of dry air in unit volume of wet air (V_{total}):

$$AD = \frac{m_{air}}{V_{total}} \tag{2.26}$$

  In regular air and assuming ideal gas, AD can be expressed as a function of gas pressures

and air temperature (T_{air}) as

$$AD = 0.028964 * \frac{P_{total} - P_w}{R_{const} T_{air}} \tag{2.27}$$

[60]

- The evaporation of water over a large surface under still room air where only natural convection is happening is given by the equation from Shah [62], [63]:

$$E = C * AD_{ws}(AD_r - AD_{ws})^{1/3}(SH_{ws} - SH_r) \tag{2.28}$$

where E is the evaporation rate per unit area expressed in kg/(m^2·h), the subscript ws refers to the condition saturated at the water surface, and r means the room condition or the environmental condition in the system far from the water surface. C is originally expressed as the equation below:

$$C = 0.14 g^{1/3} D^{2/3} \mu_{air}^{-1/3} \tag{2.29}$$

where D is the coefficient of molecular diffusivity and μ_{air} is the dynamic viscosity of air. However, C has little variation over the typical room air conditions, and can be estimated by the mean value 35 m^2/(kg$^{1/3}$h). Therefore, when calculating evaporation rate, the following equation is used:

$$E = 35 AD_{ws}(AD_r - AD_{ws})^{1/3}(SH_{ws} - SH_r) \tag{2.30}$$

This equation is derived analytically using the analogy between heat and mass transfer where the water surface is considered to be a horizontal plate with the heated face upward, and is shown to have good correlation with empirical data [64], [65].

2.4.1 Evaporation in the Top Container

When the air pathway is blocked and the decrease of pressure in the top container holds up the liquid from further filling down to the bottom container, we want to make sure that the water vapor evaporated to the top container is not going to increase the gas volume too much to allow excessive overfilling in the bottom container.

Assume that evaporation starts after the equilibrium in Eq. 2.16 is reached. Evaporation of water in the top container is going to increase the amount of water vapor, n_w, in the top container until the net evaporation rate reaches zero (RH reaches 100%). On the other hand, the amount of dry air in the top container, n_{air}, is going to stay the same. The pressure in the top container needs to stay roughly the same as both the old pressure and the new pressure need to satisfy Eq. 2.16. Although Δh in the equation will be smaller due to evaporation, the change in $\rho g \Delta h$ ($\sim$10 Pa/mm) is much smaller than P_{atm}. Therefore, in the following calculations, P_{top} is assumed to be a constant.

Applying the ideal gas law (Eq. 2.17) to water vapor and dry air separately, and assuming RH to be rh before considering evaporation, the following equation applies to the conditions before considering evaporation (Eq. 2.31) and after evaporation has reached the steady state (Eq. 2.32):

$$n_{w\_orig} = \frac{rh * P_{ws}}{P_{top} - rh * P_{ws}} n_{air} \tag{2.31}$$

$$n_{w\_new} = \frac{100\% * P_{ws}}{P_{top} - 100\% * P_{ws}} n_{air} \tag{2.32}$$

Since n_{air} stays the same, the change in the amount of gas can be expressed as

$$\Delta n_{total} = \Delta n_w = (n_{w\_new} - n_{w\_orig}) = \frac{P_{top}}{P_{top} - P_{ws}} \frac{1 - rh}{rh} n_{w\_orig} \tag{2.33}$$

Applying the ideal gas law to both n_{total} and n_{w_orig} in the above equation gives the total

volume change in the top container:

$$\Delta V_{total} = (1 - rh)\frac{P_{ws}}{P_{top} - P_{ws}} V_{orig} \tag{2.34}$$

Assume that the air temperature in the top container is 25°C, then $P_{ws} = 3168.53$Pa according to Eq. 2.23. Approximating P_{top} as 101 kPa,

$$\Delta V_{total} = 0.03238(1 - rh)V_{orig} \tag{2.35}$$

This is a less than 3.3% change of the volume of gas in the top container even if the humidity level is very low. In reality, after the initial filling cycle, the subsequent air that passes through the membrane and get into the top container is near saturation ($rh \approx 100\%$) because the bottom membrane is close to the water level in the bottom container. Therefore, in following refilling processes, ΔV_{total} is close to 0 and little overfill will occur because of evaporation.

In order to know the dynamics of the evaporation process, the following equation can be solved:

$$\frac{\mathrm{d}n_w}{\mathrm{d}t} = \frac{A_{top}}{M_w} E(n_w, t) \tag{2.36}$$

where A_{top} in our system is 47.12 mm^2 determined by the top container cross sectional area minus the straw end area, M_w is the molar mass of water, and $E(n_w, t)$ is given by

$$E(n_w, t) = 35AD_{ws}(AD_r(P_w(n_w)) - AD_{ws})^{1/3}(SH_{ws} - SH_r(P_w n_w)) \tag{2.37}$$

according to Eq. 2.30. Assuming $P_{top} = 101$ kPa, and 25°C water and air temperature, P_{ws} can be calculated from Eq. 2.23. Then AD and SH in the above equation can be calculated from pressures in Eq. 2.27 and Eq. 2.25, respectively, and P_w can be expressed as:

$$P_w = \frac{n_w}{n_w + n_{air}} P_{top} \tag{2.38}$$

Solving Eq. 2.36 numerically where the initial n_w value is calculated with the assumption that $V_{orig} = 0.8$ mL, and converting the result into gas volume gives the solutions as in Fig. 2.2. The total volume change at steady state ($t \to \infty$) in the solution is verified to be the same in Eq. 2.35.

It can be seen from the figure that evaporation reaches steady state within ∼1 min, and the total volume change is smaller than 30 µL.

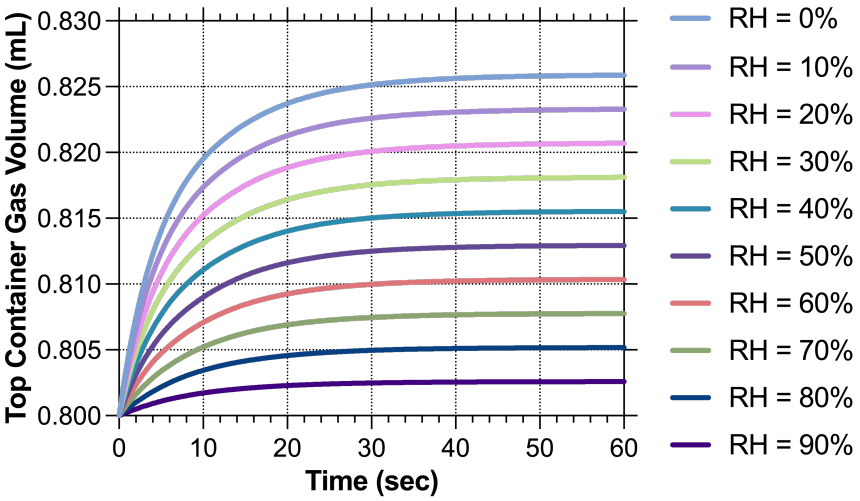

Figure 2.2: Evaporation dynamics in the top container across different humidity levels assuming an initial gas volume of 0.8 mL, an equal water and air temperature of 25 °C, and a constant total gas pressure of 101 kPa.

2.4.2 Evaporation in the Bottom Container

Since the bottom container is open to the air, the evaporation in the bottom container does not reaches steady state and can be approximated by water evaporation from a flat surface with an area, A_{bottom}, equal to the bottom container opening area. The evaporation rate per unit area calculated from Eq. 2.30 is shown in Fig. 2.3

If evaporation in the bottom container is undesired, the opening area in our design can be tuned to be very small, in which case only a small hole connects the bottom container to the atmosphere. In this way, the bottom container's evaporation rate can be made close to zero.

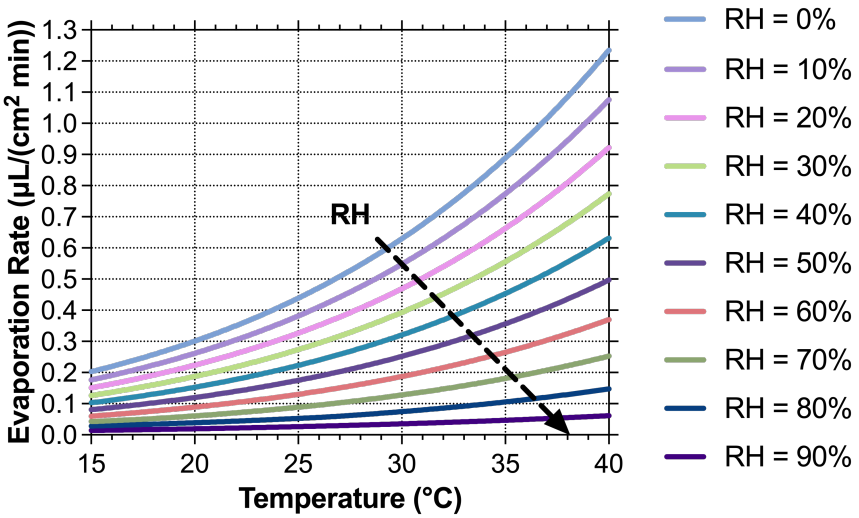

Figure 2.3: Theoretical evaporation rate per unit area across different humidity levels.

2.5 Conclusions

In this chapter, the mechanisms that drive and affect the operation of CHARM is quantitatively evaluated. Specifically, the filling and refilling rates (Eq. 2.13) depend on several parameters and changes during operation, but can be made large enough for use with flow rate required by most microfluidics. After the liquid blocks the membrane, a slight decrease (< 1 mm) in the top container liquid level is going to cause the top container gas pressure to decrease enough to hold the liquid to prevent it from overfilling the bottom container. Evaporation in the top container reaches steady state within 1 min, and causes little change in the top container gas volume. Evaporation in the bottom container depends on the opening area, but can be made small when this evaporation is unwanted.

The calculations in this chapter demonstrate in principle how the device works, and provides insights on how device parameters can affect device functioning.

Chapter 3

Device Design and Experimental Validation

3.1 Introduction

The previous two chapters have addressed the CHARM principles theoretically. In this chapter, we aimed to choose proper materials and fabrication methods for our system, build the devices physically, and test their functions as a validation for the previously discussed theories.

3.1.1 Materials and Fabrication Methods

Device Body

There are many common fabrication methods that can be used to make small intricate devices, including subtractive manufacturing, such as milling, lathing, and laser beam machining; additive manufacturing, such as 3D printing; and mass containing methods, such as injection molding and casting. Each of those fabrication methods has its own advantages and limitations. In order to choose a proper one for our design, we need to understand our design constraints on materials and fabrication methods:

- The fabricated device body needs to be air-impermeable, so that the atmospheric pressure will not influence the pressure within the top container, and no air or liquid will leak into or out of the top container. This means that the device body material itself should be air-impermeable, and that the fabrication method should not create extra gaps that allow air to pass through the device body.

- The device body finish needs to be smooth. This allows better sealing between the device body and the top container. Even with the O-ring connection, a rough material may leave gaps between the O-ring and the material, allowing air bubbles to come up into the top container during operation.

- The components need to be bio-compatible, since we want our device to work with cell culture applications, in which case the cell culture media will stay in contact with the device body during the device operation time.

- The resolution of the fabrication method should be high enough to create the fine features in the device body, including long straw structures with small inner diameters and a curved O-ring groove that needs to grip on the O-ring well.

Additionally, it will be beneficial if the device body is transparent, so that operators can see the status of liquid in the device body during operation.

Subtractive manufacturing methods can create fine details with a wide range of materials, but can be difficult to create the long straw structure with a very thin wall and a small inner diameter. Mass containing methods can produce a large number of identical parts simultaneously, but the molds are difficult to design for our system because of the straw structures.

On the other hand, additive manufacturing, mainly includes 3D printing methods, has many varieties and a wide range of capabilities. Some common forms of 3D printing include material extrusion methods (e.g. fused deposition modeling (FDM)), light polymerization

methods (e.g. stereolithography(SLA), PolyJet), and power bed fusion methods(e.g. selective laser sintering (SLS)). In our studies, these four methods were used to fabricate parts of the devices and were compared with each other before selecting the best one (PolyJet) for use with our system.

The material used for PolyJet printing was MED610^{TM}, which is transparent rigid biocompatible dental resin. Although it is ISO 10993-1 certified as biocompatible and aproved to be used as temporary in-mouth placement, the exact procedures in the certification process remains unknown. Therefore, to understand the cytotoxicity of MED610^{TM} and whether it can be used in cell culture applications, elution tests for cytotoxicity were performed.

Membrane

Besides the device bodies, the air-permeable, liquid impermeable membranes in our CHARM design are critical components of our system. It is necessary that the membrane totally blocks liquid from passing through under low pressures (<1000 Pa in our system) during the full operation time, while allowing air to pass through as freely as possible. Porous polytetrafluoroethylene (PTFE) membranes have such properties and were used in our system. POREX Virtek® has several PTFE membrane options with different thickness and air permeability. They also have different Ingress Protection (IP) ratings, indicating the extent of water protection. Depending on the system to be used, different membranes can be chosen.

In our experiments, two membranes were tested (PMV10 and PMV25). PMV10 has a higher air permeability, with a typical airflow of 107 L/hr/cm^2 under 70 mbar (7000 Pa), but does not provide long term protection against water (IP rating 64, 67), while PMV25 has a lower air permeability with a typical airflow of 17 L/hr/cm^2 under the same pressure condition, but provides protection against immersion in water under pressure for long periods (IP rating 65, 67, 68).

Membrane-Straw Sealing

The membrane-straw integration method was the next to be considered. PTFE's extreme chemical resistance and chemical inertness make it difficult to adhere to other materials[66]. Ways to adhere PTFE to another material include thermal welding (or other welding methods that produce heat such as ultrasonic welding), and adhesive bonding [67]. Both methods were explored and adhesive bonding was chosen to be used in our system.

3.1.2 Functional Validations

Finally, with the device assembled, the device operation was tested to see if the liquid level could be maintained for a long period of time (∼2 days), and if the previously calculated filling/refilling rates and evaporation rates were valid.

3.2 Materials and Methods

3.2.1 Device Body Fabrication Method Comparison

Straw structures of the size to be used with our system (∼2 mm ID, ∼3.2 mm OD) were made with 3D printing methods including FDM (from Prusa i3 MK3 3D Printer using polylactic acid (PLA)), SLS (from Xometry® using nylon 12 with vapor smoothing surface finish), SLA (from ELEGOO Saturn 2 printer using ELEGOO 8K Standard Resin), and PolyJet (from Stratasys J5 printer using Stratasys MED610™ resin). The appearances of the fabricated structures were visually compared and PolyJet with MED610™ was chosen to be the fabrication method for device bodies in our system.

3.2.2 Cytotoxicity Test

To evaluate the feasibility of using the device in cell culture applications, an elution test was performed to assess the cytotoxicity of the 3D printing material MED610™ where the

target material was extracted in cell culture media with serum which was later used to grow cells.

Polypropylene is a plastic widely used in tissue cultures and has been shown to have little or no adverse effects for cell cultures. [68] In this experiment, polypropylene was used as a negative control material to compare with MED610^{TM}'s cytotoxicity. The MED610^{TM} used in the experiments were in the shapes of 4 device bodies, while the polypropylene was used in 4 tubing shapes that were cut to the length of the device bodies plus some extra small pieces to make the total surface area roughly equal to the MED610^{TM}'s surface area. A no material control and a fresh media control were also included.

The media used was Dulbecco's Modified Eagle Medium (Gibco, cat#11960044) supplemented with 10% FBS (Gibco cat#16140071), 2% L-glutamine (Gibco cat#25030081), and 1% penicillin-streptomycin (Gibco cat#15140122).

The following cleaning procedures were done to the materials:

1. Sonicate in 70% ethanol for 30 min.
2. Soak in new 70% ethanol at room temperature for 6 days.
3. Rinse with sterile deionized (DI) water once.
4. Sonicate in new sterile DI water for 30 min.
5. Rinse with new sterile DI water for 3 times.
6. Soak in media in 37 °C incubator for 5 days.

After the cleaning procedures, the MED610^{TM} and polypropylene materials were submerged in 40 mL new media, separately, and placed in the 37 °C incubator for 7 days together with another 40 mL of no material control media.

All media was then aliquoted into 7 day's use as cell culture replacement media and stored in a 4°C fridge before use (3 days before the use of Day 1 media.) The fresh media

was also aliquoted into the same amount as the other 3 conditions. Together, there were 4 differently conditioned media, being

- MED610^{TM} media
- Polypropylene media
- No material control media
- Fresh control media

3T3 cells (passage # 9) were used for testing those media. Cells were seeded into 16 wells (4 replicates for each condition) in the middle of a 48 well plate in 300 µL fresh media with an initial density of 7500 cells/well. The region surrounding the 16 wells were filled with 300 uL of Dulbecco's Phosphate-Buffered Saline (DPBS) to create similar humidity environments for the cell culture wells.

On each day starting from the next day (day 1) after seeding, phase images were taken using Nikon Eclipse Ti-E microscope under both 4x and 10x objectives, and media in each well was replaced with new warmed conditioned media.

Cell counts were generated from the 4x images by the software iCLOTS [69].

3.2.3 Membrane Sealing Methods Comparison and Pressure Test

Initially, the thermal welding method was tested to see if the PTFE membrane can be attached to plastic materials, including thermoplastics (PLA and nylon 12) and thermoset resins (ELEGOO 8K Standard Resin and MED610^{TM}). PMV25 membranes were used in the test. The setup of thermal welding is shown in Fig. 3.1. A soldering ion was heated and used to press the membrane on the straw structure of the material to be tested.

Subsequently, the adhesive bonding method was tested on MED610^{TM}. As the straw wall thickness ($<$ 1mm) was too small for tape adhesives to properly attach, we used liquid glues for testing, including super glue (Loctite Super Glue Gel Control), epoxy glue (Loctite

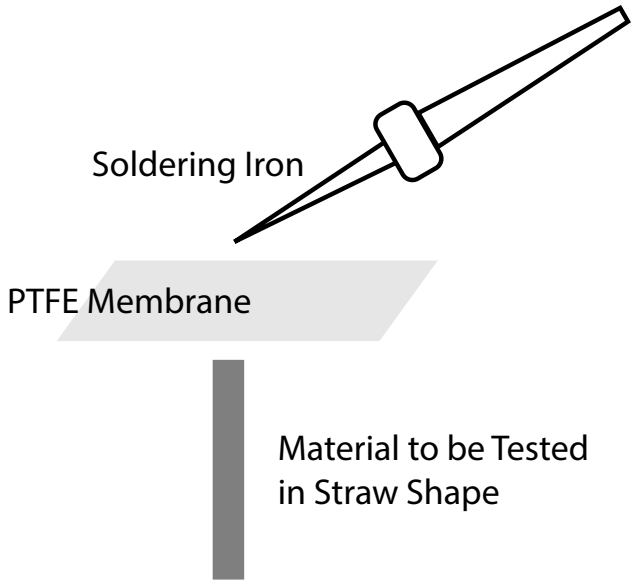

Figure 3.1: Thermal welding test setup. A soldering iron was heated and used to press the membrane onto the material to be tested with a straw structure.

Epoxy Quick Set), and UV glue (Bondic Pro UV Resin). In order to spread an even layer of certain amount of glue on the straw end, a rectangular sheet with holes of different depths were printed (using PolyJet), and glue was spread to fill the hole before dipping in the straw vertically. After that, the straw was pressed on the membrane without slipping to allow precise attachment. After the glue dried (or shining UV light on the UV glue), the membrane hanging around was cut out. The entire process is shown in Fig. 3.2.

The connection integrity was first investigated by peeling off the membrane using a set of tweezers. If the membrane could be peeled off easily, then the bonding was too weak.

To further test if the membrane attachment was strong enough to prevent liquid from going through under the conditions required by our system, pressure tests were performed.

After membrane integration on one end of the straw, a 1 mL syringe with colored water in it was attached to the other end of the straw and sealed using UV glue (Fig. 3.3). The syringe was pushed by hand with a gradually increasing force to exert an increasing pressure on the membrane and the membrane-straw seal, until either the membrane or the membrane-straw seal failed (liquid came through). The tests were repeated 5 times for each condition.

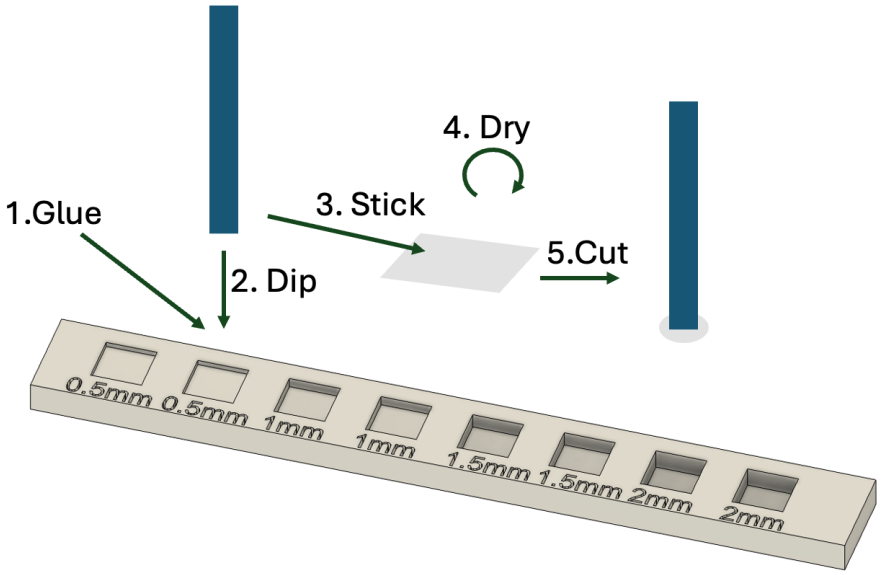

Figure 3.2: Adhesive gluing method for attaching PTFE membrane to straw end. 1. Spread out glue to fill the hole of certain depth; 2. Dip the straw end in the glue and take out vertically; 3. Press the straw end on the membrane to stick to it; 4. Wait until the glue fully dries/cures; 5. Cut out the membrane hanging around.

3.2.4 Functional Validation

The devices were made and assembled according to Fig. 1.5a. The device bodies and the top containers were 3D printed using the PolyJet method with MED610^{TM} resin using Stratasys J5 printer. Longer devices and top containers and wider bottom containers (15.5 cm ID, 18 cm OD glass tubes) were used for the functional testing to amplify the effects that can be observed. The widths/diameters of the device bodies and top containers were kept the same as the ones used on 96 well plates. The device length dimensions are shown in Fig. 3.4.

The membrane was attached to both ends of the air straw with super glue (Loctite Super Glue Gel Control) using the method described in Section 3.2.3 with glue depth of 0.5 mm, except that the membrane was punched into 3 mm discs first, and then stuck to the straw end. This ensured that there was no extra membrane hanging around.

When inserting the device bodies into the top containers, an O-ring was replaced by UV glue that fully sealed the connections permanently because the proper size of the O-ring had

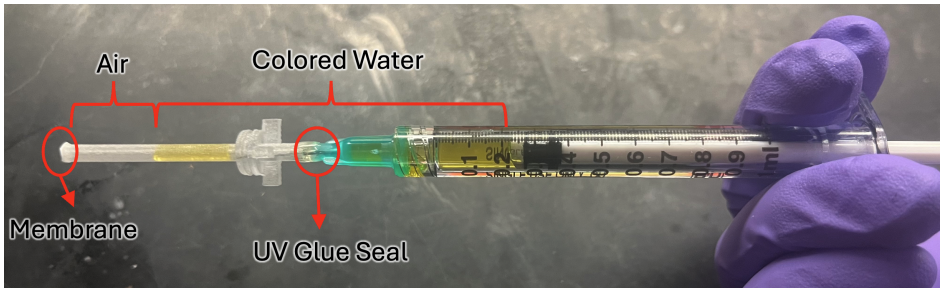

Figure 3.3: Membrane sealing pressure test setup. A syringe with colored water is attached to one end of a straw sealed by membrane on the other end. The liquid was pushed towards the membrane manually.

not been tuned to be good enough to fully seal the top container.

Water to be used in the experiment was room-temperature, and was mixed with yellow food color for better visualization. The bottom container was filled with water to a level below the membrane but not too far away from the membrane. Water was then injected into the top container from the liquid straw using a syringe. After placing the devices in their correct orientations on top of the bottom container, water started to go down through the liquid straw. The whole filling and refilling processes were videoed using a time-lapse camera with one image taken every 10 seconds, until the devices stopped filling down liquid. The air temperature and relative humidity level around the device was videoed together. One frame from the video showing the whole testing scenario was shown in Fig. 3.5.

The liquid heights over the testing period were extracted from the videos and analyzed. The water levels were extracted by sensing the change in average RGB values over the entire top/bottom container diameters. The filling and refilling periods were identified, and the fluctuations in the liquid levels in the bottoms container were calculated. Volume changes in the top and bottom containers were converted from the liquid heights and container areas, and the total volume changes were compared with theoretical evaporation calculated from Eq. 2.30 using the measured temperature and relative humidity, assuming water and air temperature to be equal. The volumetric filling and refilling rates were calculated from the slopes of least squares linear fits of the volume changes over time, and were then plotted against the sum of the top container liquid height and the liquid straw height at the middle

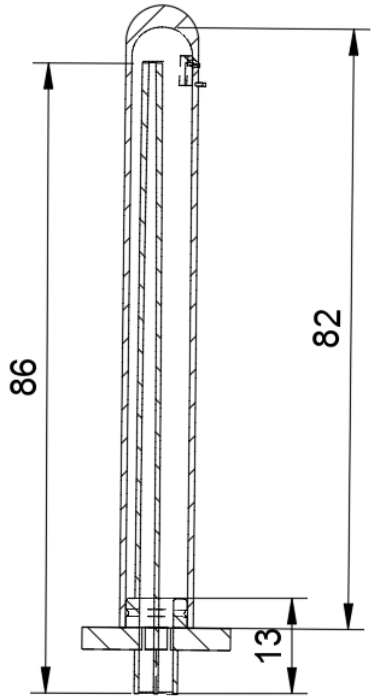

Figure 3.4: Device dimensions used for functional tests. Numbers are in mm.

time of the fitting range for verification of linear relationship.

The filling rates were also measured with the original autofiller's setup in Fig. 1.4 (without microfluidic chip and outlet container). The membrane with adhesive was stuck to a cylindrical PDMS connector, and then attached to the bottom of the tubing, as shown in Fig. 3.6c. A tight seal between components was created by applying epoxy glue to the sanded surfaces of the connection points. Two flow setups were tested, one using 50 mL Falcon tubes as top and bottom containers and 0.0625" ID Tygon® tubing as the liquid and air straws, and the other one using 15 mL Falcon tubes and 0.02" ID, Tygon® tubing (Fig. 3.6).

The liquid heights in the top and bottom containers were measured over time until the bottom container liquid level stopped at the membrane, and then the volumetric rates were calculated.

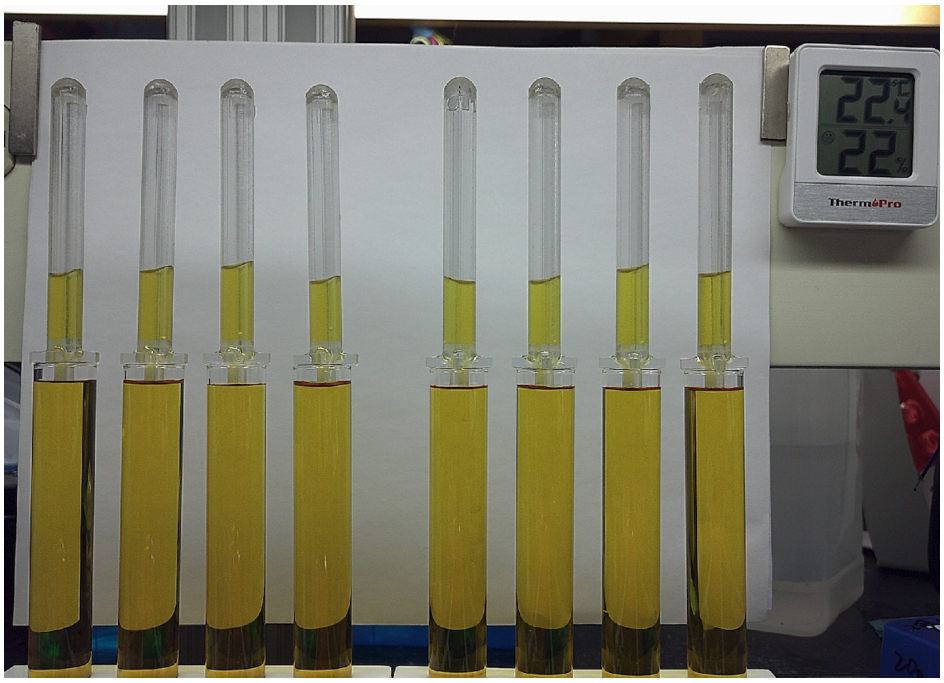

Figure 3.5: Device functional test setup showing one frame captured by the time-lapse camera with 8 devices and the temperature and humidity measurement.

3.3 Results and Discussion

3.3.1 Materials and Device Fabrication

The images of the device straw structures fabricated with different 3D printing methods are shown in Fig. 3.7. The FDM method joined extruded thermoplastic filaments layer by layer, but the connections between filaments left gaps in between, and the created straw walls were wiggly (Fig. 3.7a). The SLS method fused powder using heat created by laser, and was able to preserve the shape of the straws, but even after vapor smoothing, which was supposed to smooth and seal the device surfaces, the straw walls still appeared to be porous (Fig. 3.7b), which may be due to the limited access of vapor within the straw. The SLA method used UV lights to fuse liquid resin layer by layer in a big resin bath, and was able to create very smooth surfaces, but the straw inner opening tended to be blocked (not shown in Figures). On the other hand, the PolyJet method deposited and fused resin layer by layer

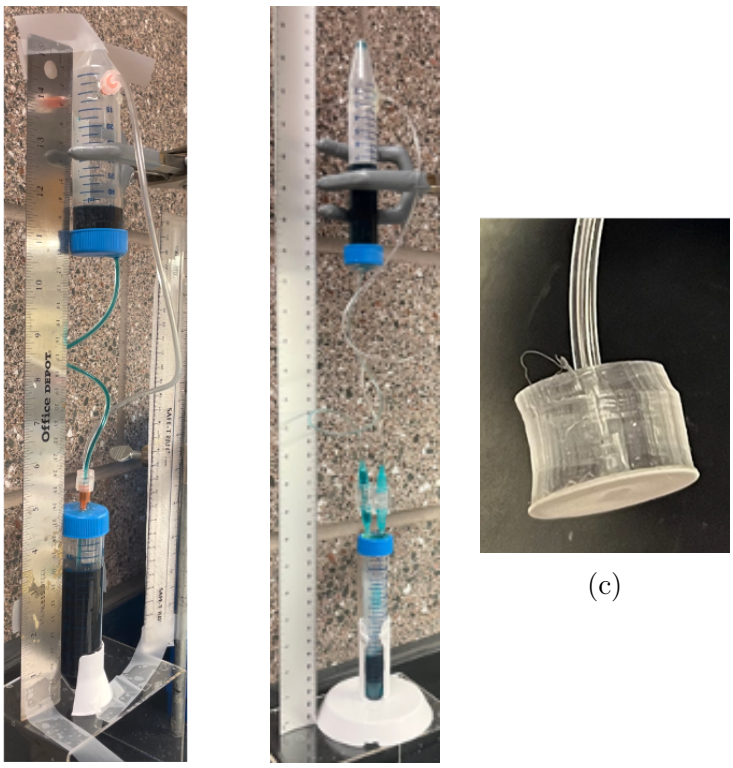

(a) (b) (c)

Figure 3.6: Two autofiller tests setup using different sizes of containers and straws. (a) Setup with 50 mL Falcon tubes as containers and 0.04" ID, 0.08" OD Tygon® tubing as the straws. (b) Setup with 15 mL Falcon tubes as containers and 0.02" ID, 0.04" OD Tygon® tubing as the straws. (c) Cylindrical PDMS connector allowed membrane attachment to the tubing.

on a clear build base, and was able to preserve the wall shapes without generating pores and create a very flat straw bottom (Fig. 3.7c), providing benefits for membrane integration. Therefore, among the four methods, only PolyJet meets the design constraints as described in the Introduction Section, so it was used to make whole device bodies in the subsequent experiments.

In fact, during the early testing stages of the module, the porosity issue was not attended, and devices made with Nylon 12 by SLS were used in functional testing. Although those devices initially appeared to maintain the liquid level in the bottom container, over time overfill would occur (observable after a few hours of operation). The overfill indicated that air was slowly getting into the top container, allowing liquid to slowly drain down. This slow overfill happened even with devices where the top container-device body connection was sealed with

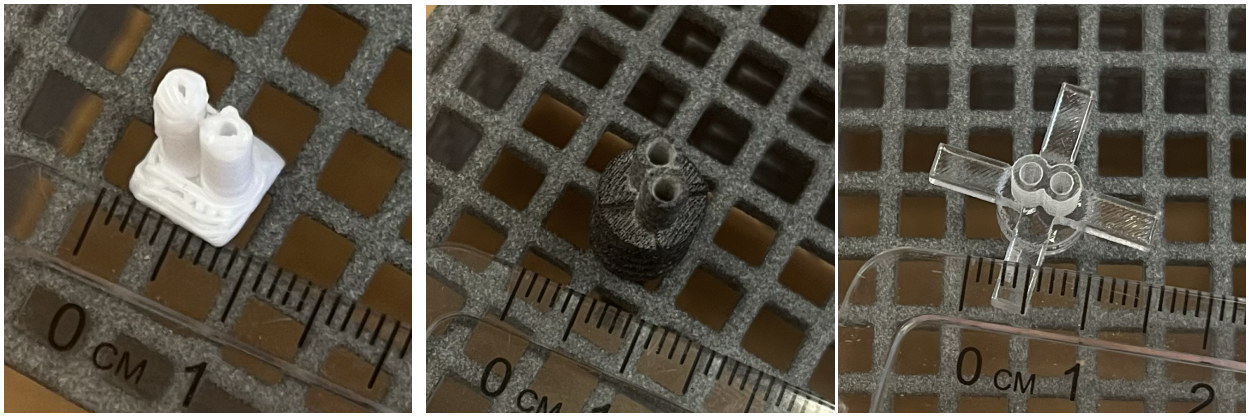

(a) (b) (c)

Figure 3.7: Straw structures fabricated using three different 3D printing methods. (a) Made by FDM with Polylactic Acid (PLA). Wall structures were wiggly and not well preserved. (b) Made by SLS (with vapor smoothing) with Nylon 12. Wall structures were preserved but are porous. (c) Made by polyjet with MED610^{TM}. Wall structures were well preserved, no pores were observed, and the straw ends were smooth and even.

vacuum grease. Therefore, we hypothesized that air was getting up through the pores in the device bodies. Also, the devices would stop filling if reused after ∼1 day of operation. This indicated that the air pathway was blocked, so no liquid could drain down from the bottom container. After cutting the air straw, liquid was observed within the air straw, which was abnormal because both ends of the straws were sealed by liquid-impermeable membranes. After making sure that the membrane-straw seal was liquid impermeable as described in the pressure test results section below, we hypothesized that the liquid came through the device bodies, which were porous. After switching to the nonporous MED610^{TM} devices, the successes in functional testing (as described in the functional testing results section) confirmed our hypotheses.

3.3.2 Cytotoxicity Test

The cell counts during the 7 day cytotoxicity test are shown in Fig. 3.8. It can be seen that cell counts under all conditions grow from a similar initial number to a similar final number, although the growth rates are not all the same. From day 5 to day 7, cells in all conditions

were at confluency. This can also be examined from the representative phase images in Fig. 3.9. Cells were sparse on day 1, but all reached 100% confluency on day 5.

From Fig. 3.8, the fresh control condition grew the fastest, which was expected. The MED610^{TM} condition grew at a similiar speed with the no material control. Therefore, no adverse effects for cell growth were found for media in contact with the MED610^{TM} material for 7 days, and the results provided support for the validity of using the material for cell culture applications.

However, it can also be observed that the PP condition grew at a speed faster than the no material control group, while it was expected to grow similarly to the no material control. This faster growth may be due to the variations in the initial sell seeding density, and more tests need to be performed to verify this hypothesis.

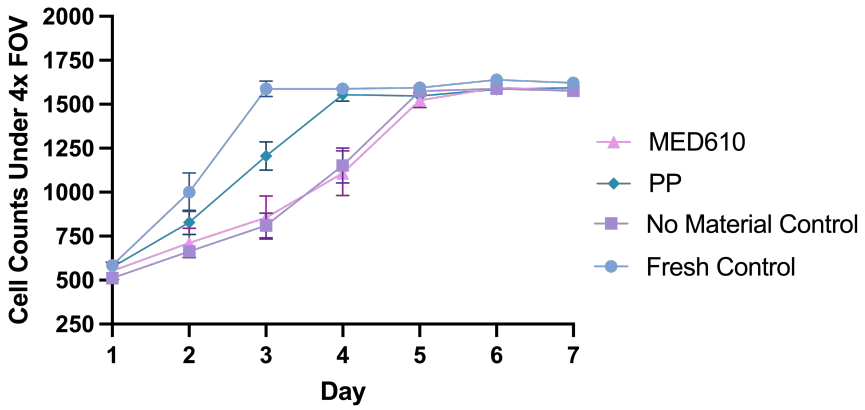

Figure 3.8: Cell counts from phase images under 4x field of view (FOV) generated by iCLOTS [69] from the 7-day cytotoxicity test. n = 4.

3.3.3 Membrane Sealing Methods Comparison and Pressure Test

The thermal welding method on PLA and nylon 12, and the adhesive bonding method on MED610^{TM} created bonds that were not easily peelable by the tweezers and showed good results in the pressure test as described later below.

The thermal welding method did not stick the membrane to the resin materials at all, and only created bonds with thermoplastic materials. This is probably because during thermal

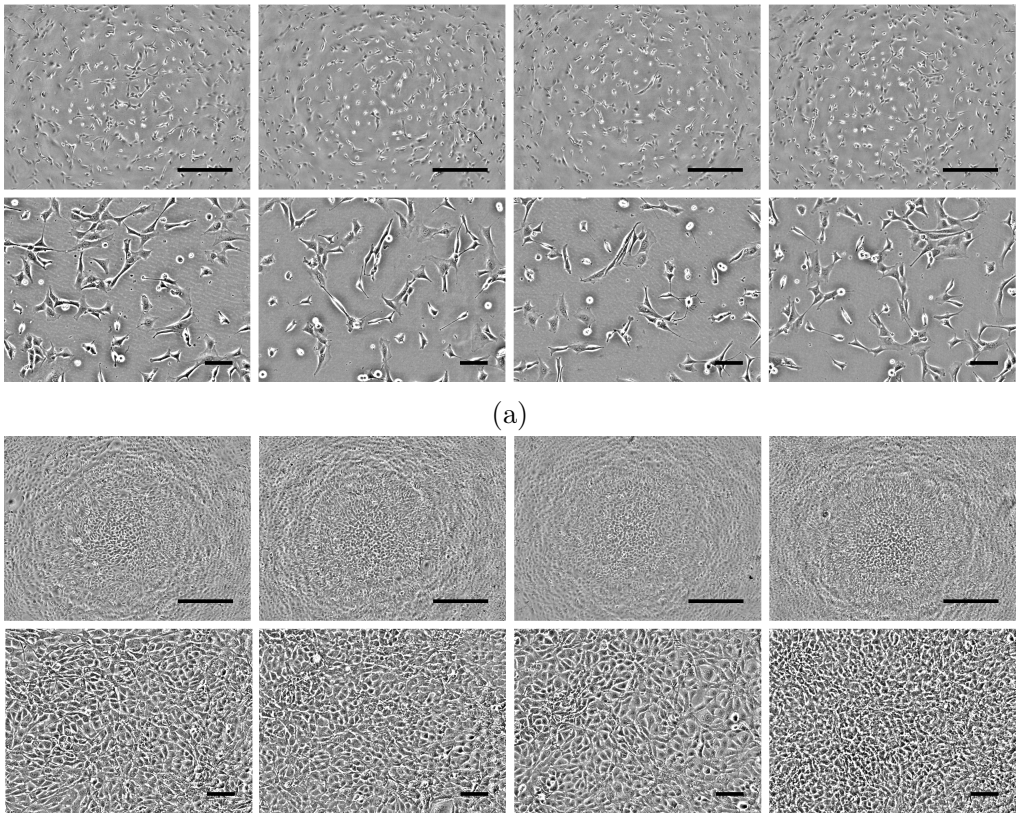

(a)

(b)

Figure 3.9: Representative phase images from the cytotoxicity test. For each row of image from left to right, the images are from the MED610^{TM}, PP, no material control, and fresh control conditions. The 4 images in each column are from the same well. All images were processed with contrast and brightness adjustments and background removal (by subtracting low-frequencies from the images). (a) Day 1 images under 4x (top row, scale bar = 500 µm) and 10x (bottom row, scale bar = 100 µm). (b) Day 5 images under 4x (top row, scale bar = 500 µm) and 10x (bottom row, scale bar = 100 µm).

welding, the thermoplastic material melted at the places that were heated, and the melted molecules got intertwined with the PTFE membrane molecules, creating a connection. The resin materials are thermoset, and would not melt under heat. Since MED610^{TM} is a resin, the thermal welding method could not work.

Therefore, adhesive bonding methods were then tested on MED610^{TM}. The epoxy glue was too viscous and tend to block the membrane totally, and UV glue created a weak bond that was easily broken by peeling with tweezers. However, the super glue was able to create a strong bond. The texture of the used super glue was neither too viscous nor too non-viscous.

At depths of 0.5 mm, the glue sticks to the straw end without blocking it most of the time. At higher depths, the glue could block the straw end, which needed to be wiped out using a blunt needle. Therefore, the 0.5 mm depth of super glue was used for the pressure tests and the later functional validation.

During the pressure test for thermal welding methods for thermoplastics and for adhesive methods for MED610^{TM}, initially, air remaining in the straws was pushed out from the membranes freely. This was expected because the membrane was air-permeable. When the air in the straw got depleted, a sudden rise in the resistance was felt from the syringe end. After increasing the pushing force, the liquid came through the middle of the membrane, not through the membrane-straw seal for all tests (Fig. 3.10). The results suggested that the seal between the membrane and the straw was intact below the water entry pressure of the membrane (750 mbar for PMV25).

From the results, the thermal welding method can be used for the tested thermoplastics, while the adhesive method with super glue can be used with MED610^{TM}.

In fact, if the printing method could be improved for the FDM or SLS methods to solve the air-leaking issue, the thermal method could be used in real devices. However, we continued with adhesive gluing on MED610^{TM}, and the improvements on other 3D printing methods remained to be investigated in the future.

3.3.4 Functional Validation

To validate our system's ability to maintain a constant liquid level, and to characterize our devices' working conditions, devices operating for ∼2 days were videoed and the following results were obtained.

The detecting regions for top and bottom water levels and the extracted levels in one frame were shown in Fig. 3.11. The liquid heights relative to the bottom of the top container over the 45-hour testing time are shown in Fig. 3.12a. From the top container liquid level change, the initial filling cycle and the subsequent refilling cycles were identified and labeled.

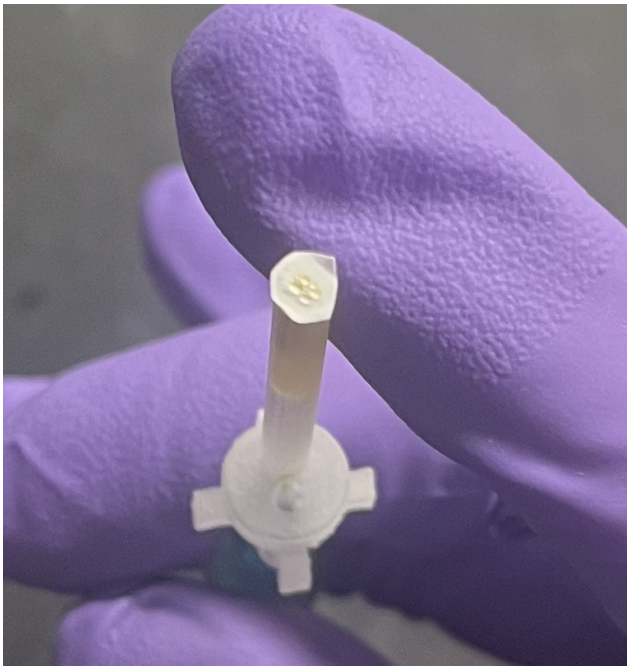

Figure 3.10: Membrane sealing pressure test result. The liquid went through the middle of the membrane but not through the sealing between the membrane and the straw.

During each cycle, the water in the top container filled to the bottom container until the bottom container liquid level reached the membrane, and then stayed constant for a period of time until evaporation decreased the bottom container liquid to open up the membrane. After the initial filling (in cycle 0), the liquid level in the bottom container fluctuated slightly (< 1.12 mm) but stayed relatively constant at the membrane level on the straw bottom. After refilling cycle 6, the liquid in the top container ran out and the bottom container liquid level gradually decreased due to evaporation.

The volume changes for the same device were shown in Fig. 3.12b. Using linear regression fits, the experimental evaporation rate was calculated to be 34 µL/hr, while the theoretical evaporation rate had an average of 14 µL/hr under the experimental conditions. The two values had discrepancies, but were on the same order of magnitude.

We hypothesized that the discrepancy between the experimental and theoretical evaporation rate might be due to the fact that the bottom evaporation surface area was small. In such cases, the edge effects started to be in-negligible as the humidity around the edge was

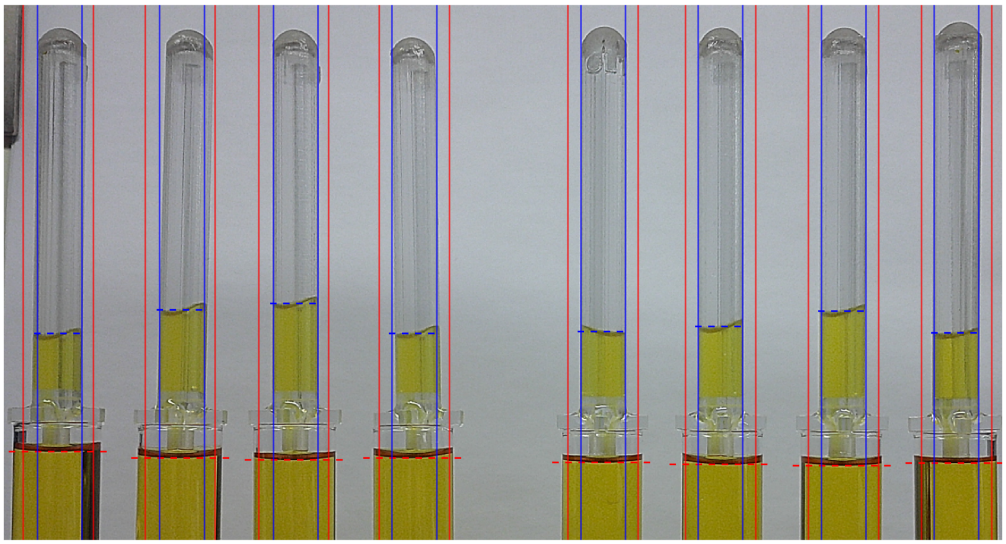

Figure 3.11: Region of detection for water levels and detected water levels in one frame. The blue lines show the regions and levels for the top container liquid, while the red lines show those for the bottom container liquid.

lower than the humidity it would be if the bottom were also surrounded by liquid. Also, the room air velocity was not exactly zero because of the ventilation system in the room and the lab personnel walking around. Therefore, the measured evaporation rate was higher than the theoretical evaporation rate.

For better visualization of the processes, the zoom-in views during the initial filling and the subsequent refilling cycle 1 were shown in Fig. 3.13, with a device liquid level visualization for two points during the refilling cycle.

The initial filling processes were divided into 12 regions having the same durations. For each two consecutive regions, a linear fit was performed to calculate the filling rate, and the sum of the top container liquid height (h_{top}) and the liquid straw height ($L = 13$ mm) at the middle of the two regions were recorded, resulting in 10 pairs of filling rates vs. heights values.

During each refilling cycle, since the refilling duration and liquid height changes were small, one linear fit was performed, and $h_{top} + L$ at the middle time was recorded.

The filling and refilling rates collected in different devices with PMV10 and PMV25 membranes were shown in Fig. 3.14a, and 3.14b, respectively.

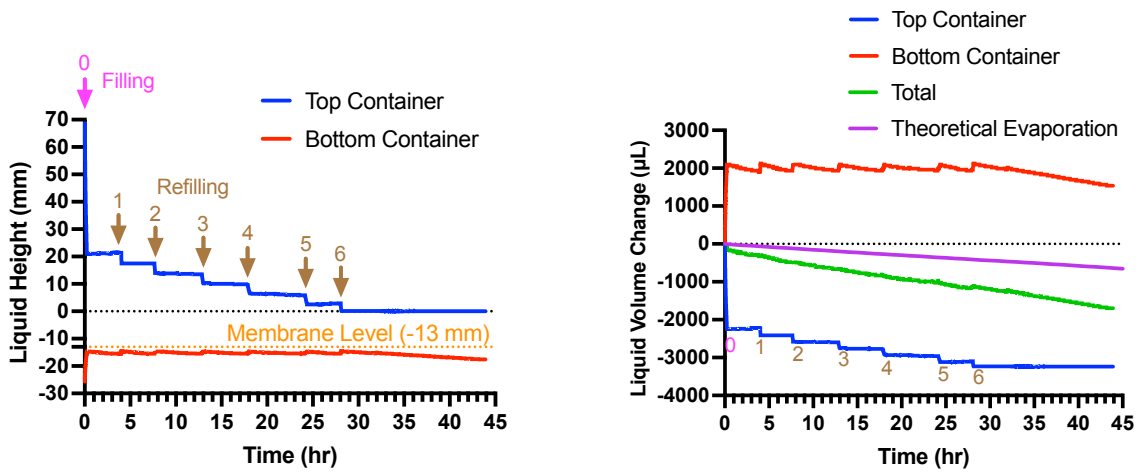

(a) (b)

Figure 3.12: Representative liquid height and volume development for the device functional test over 45 hours showing the full operational stages of the device. (a) Liquid heights relative to the bottom of the top container. The magenta arrow shows the start of the initial filling cycle, and the brown arrows show the starts of the refilling cycles. (b) Volume changes compared to the initial volumes. The volume changes for the top and bottom container liquid were converted from the measured height changes. The total volume is the sum of the top and bottom container liquid volume changes, and represents the total liquid evaporation from the system.

As can be seen in both figures, the filling/refilling rates showed a linear relationship with regard to $h_{top} + L$, supporting the relationship calculated in Eq. 2.13. The devices with PMV10 membranes had an average slope of 25 µL/min/mm, while the devices with PMV25 membranes had an average slope of 3.6 µL/min/mm. This suggested that the resistance of the PMV10 membrane was around 1/7 of that of PMV25 under the operating range of pressure (around $0 \sim 800$ Pa). From the membrane specifications, the typical air flow rates of PMV10 are around 6.3 times as high as those of PMV25 under 70 mbar (7000 Pa), indicating that the resistance ratio is around 1/6.3, which is close to our measured ratio.

The refilling rates were sometimes lower than expected by the linear relationship from the filling rates, especially for the data shown in orange dots in Fig. 3.14a. This was probably because there was still some liquid retaining on the membrane when the liquid level dropped in the bottom container, resulting in a higher membrane resistance, as predicted in Sec 2.2.

The initial filling rates for the autofiller setup also showed an expected linear relationship

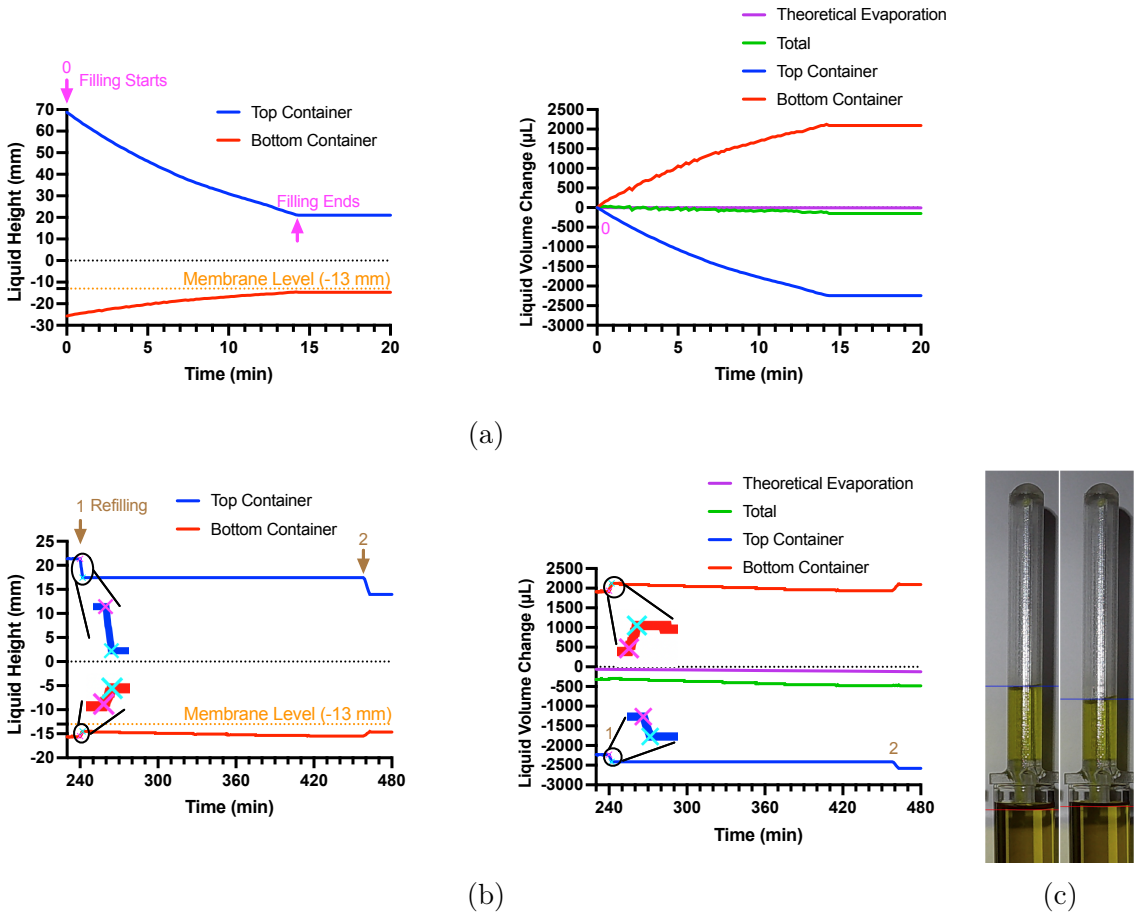

Figure 3.13: Representative liquid height and volume development for the device functional test over 45 hours showing the full operational stages of the device. (a) Zoom-in views for the initial filling cycle. (b) Zoom-in views for the refilling cycle 1. (c) Device appearance at points specified in (c). The left image shows the appearance immediately before refilling (magenta cross as shown in (b)), and the right image shows the appearance immediately after refilling (cyan cross).

with the liquid height difference between the top container and bottom container levels (Fig. 3.15). Linear fits were done on the experimental data forcing the line to go through the origins, and were compared with the calculated relationships (also shown in the figure) obtained from Eq. 2.11, which assumed no membrane resistance. $h_{top}+L$ in the equation was replaced by the height difference between the liquid levels in the top and bottom containers because the liquid straw extended towards the bottom of the bottom container as shown in Fig. 1.4. The calculated filling rates were larger than the experimental filling rates, which were expected due to membrane resistance.

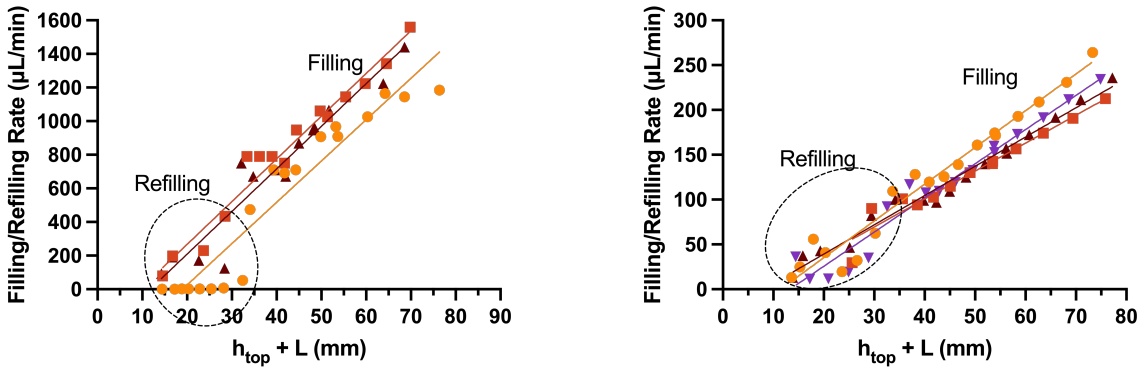

(a) (b)

Figure 3.14: Filling and refilling rates measured from different devices and their relationship with liquid heights. The data points in the dashed circle represent the refilling rates, while the other ones represent filling rates. (a) Tested with devices with PMV10 membrane. Data from 3 different devices and their least squares linear fits are shown in different colors. (b) Tested with devices with PMV25 membrane. Data from 4 different devices and their least squares linear fits are shown in different colors.

An interesting observation during functional testing for CHARM setup was that when the membranes were stuck to the straw bottom first and then cut (instead of punched out and then stuck to the straw bottom), another water level pattern usually appeared as shown in Fig. 3.16.

Initially, the liquid in the top container filled down similarly (stage 1). However, the blockage of the membrane bottom did not fully stop the liquid filling, and a slower rate of overfilling was observed, indicating that some air was slowly getting into the top container (stage 2). After the overfilling reached certain height, the overfilling stopped, and a no-fill stage (stage 3) started, which indicated that the air pathway was now blocked. After the bottom liquid level dropped down, a continuous refilling stage (stage 4) began, indicating that air was slowly but continuously filling into the top container. In this stage, the bottom water height stayed roughly constant, indicating that the refilling rate roughly equaled to the evaporation rate. In the end, the top container liquid ran out and the refilling stopped (stage 5).

We hypothesized that this behavior was because the membrane hanging around the

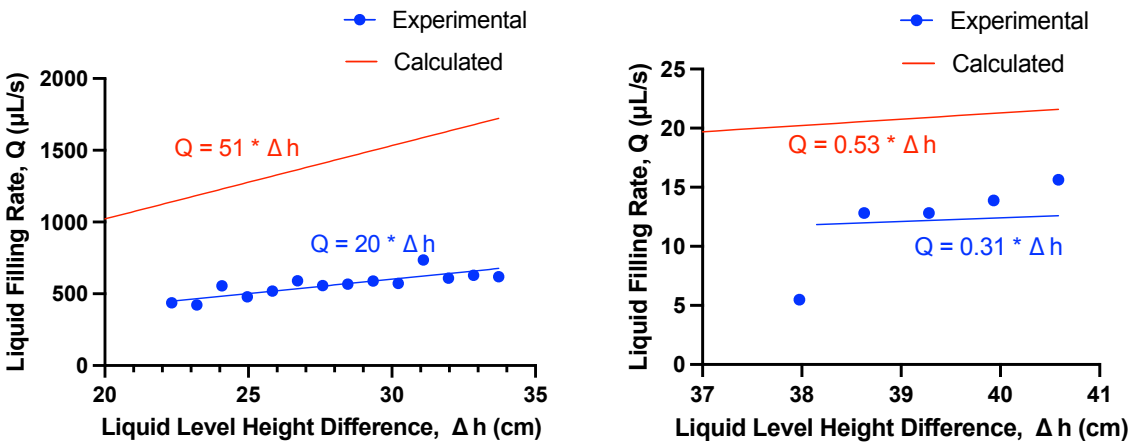

(a) (b)

Figure 3.15: Autofiller filling rates test results indicating linear relationship between the liquid filling rates and the height differences between the top and bottom container liquid levels. The calculated filling rates were based on Eq. 2.11 without considering the membrane resistance, where $h_{top} + L$ was replaced by Δh. (a) Setup using 0.0625" ID tubing and 50 mL Falcon tubes as containers. (b) Setup using 0.02" ID tubing and 15 mL Falcon tubes as containers.

edge of the straw created extra areas for air to enter the straw through membrane sideways (Fig. 3.17). If the membrane was punched to the shape first, the edge of the membrane would be sealed by glue when sticking the membrane on the straw end. On the other hand, if the membrane was stuck to the straw bottom first, the edge of the membrane and any excessive regions left behind the cut will expose membrane to the air and allow air to pass through sideways. Therefore, when the liquid blocked the bottom entry of air, air could still enter the top container slowly, causing a slow overfilling. When the overfilling made the bottom liquid level high enough to block the sideway entries, no air could enter the top container and the no-fill stage began. Afterwards, evaporation gradually exposed some membrane area, and refilling gradually occurred until the refilling rate approximately equal to the evaporation rate, which explained what happened in the refilling stage. This hypothesis can be tested in the future by adding an extra step after the stick-cut method: use glue to seal the membrane edge and then test the device functioning.

In fact even with the side entry issue, the liquid level stayed relatively constant after the

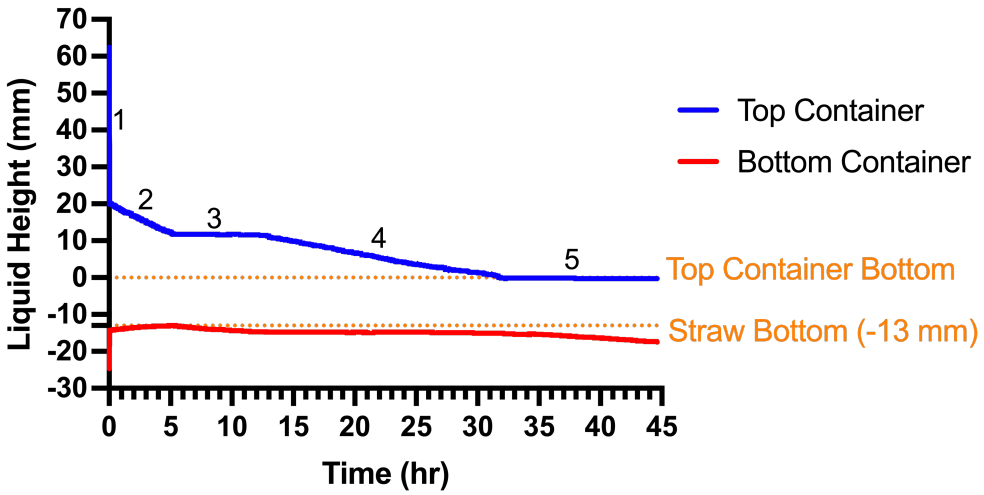

Figure 3.16: Liquid heights over 45 hours in devices with membranes stuck first and cut later. Five stages were observed: 1. Fast filling; 2. Slow overfilling; 3. No filling; 4. Slower continuous filling; 5. Top container liquid ran out.

initial water filling. The total fluctuation after the initial filling and before the top container liquid ran out was ∼1.54 mm. Therefore, for systems that do not accuracies below 1.54 mm, the stick-cut method for membrane integration can be applied too.

3.4 Conclusions

In this chapter, device materials and fabrication methods were compared and PolyJet printing method with MED610^{TM} material was chosen for our CHARM system. Pressure tests indicated strong attachment of membrane with straw bottom using super glue, and material cytotoxicity tests supported our devices' use on cell culture applications. Functional tests support the previously calculated relationships and confirmed the main purpose for the design: maintain a constant hydraulic head for a long period of time.

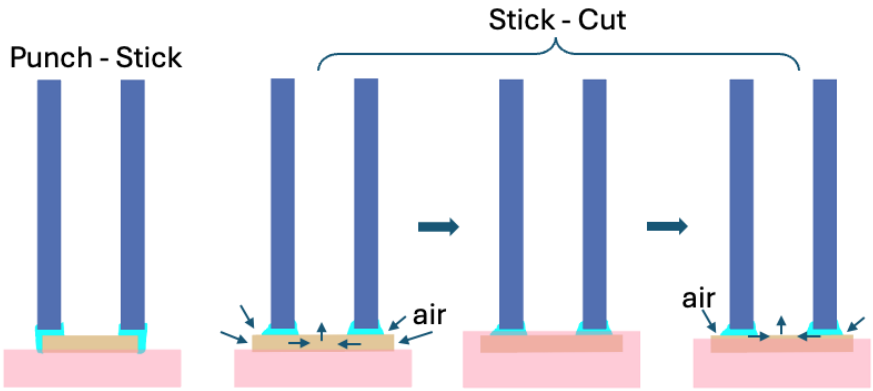

Figure 3.17: Hypothesis illustration for behavior differences of different membrane integration methods caused by air entering the membrane sideways. The glue was shown in cyan, membrane in light apricot, straw walls in blue, and water in pink. The punch-stick method blocks the side of the membrane, while the stick-cut method creates extra areas that allow air side entry. The three steps for the stick-cut method indicated the status during the overfilling, no filling, and coninuous refilling stages, respectively.

Chapter 4

Contributions and Future Directions

4.1 Conclusions and Contributions

In this thesis, a constant fluid level maintainer, CHARM, was developed for use on gravity-driven flow microfluidics that require a constant driving force. We discussed the working principles of the module in theory quantitatively (Chapter 2), chose and validated the device materials and fabrication methods (Chapter 3), and confirmed the working principles by the functional tests on fabricated devices (Chapter 3).

The module was able to keep the variations of the fluid level at the microfluidic inlet port below 1.1 mm until the liquid supply ran out without human intervention, which corresponded to a pressure variation of 11 Pascals within the 30-hour demonstrated operation time. Therefore, this module is suitable for gravity-driven microfluidics requiring a constant driving force with tolerances larger than 11 Pascals. The filling/refilling rates that the module was able to achieve varied linearly with the remaining liquid height in the top container, but the average highest and lowest rates for devices with PMV10 membrane were 1394 µL/min and 57 µL/min, and those with PMV25 membrane were 237 µL/min and 23 µL/min. Since the filling/refilling rates need to be larger than the microfluidic chip flow rate for the module to work properly, researchers using the module can choose the appropriate

membrane that allow the necessary flow rate for their microfluidic chip. The opening area of the bottom container can be made small to decrease evaporation, or can be made large to allow easy access to the bottom container liquid, but in the latter case the evaporation rates with edge effects need to be subtracted from the filling/refilling rates when considering the membrane to be used.

There are many features of the design that we are proud of which holds significance to the scientific community. Firstly, the compactness of the design ensures that the entire module can be simply placed on top of microfluidic ports as small as the wells in 96-well plates, and that researchers can run parallelized and high-throughput experiments easily with the help of our devices. This feature holds advantages against the other flow regulation methods as described in Chapter 1, and can greatly increase the working efficiencies for microfluidic users.

Secondly, the simplicity of the fabrication and operation processes lowers the technical barriers for new researchers to put the technique into use. Moreover, the tubing-free design increases the robustness of the system and reduces the setup time before operation. Together, these features contributes to the user-friendliness of our system, which is one of the fundamental requirements for a system to be widely adapted.

Lastly, our design is compatible with cell culture applications that require a stable media perfusion, which creates shear stress on the cells and enhances cell growth [7], [8]. Therefore, our device can not only be used on platforms for physical or chemical processes such as particle separation or drug synthesis, but also be used with biological processes such as cell or organoid growth. Cell biology is a popular field in microfluidics, and we are glad that our system can contribute to researches in this area.

4.2 Future Work

It was mentioned in the functional test results that the membrane needed to be punched into its circular shape before stuck to the straw bottom, and a membrane side-entry hypothesis was proposed. In the future, this hypothesis can be tested by using the stick-cut membrane integration method with an additional gluing step that blocks the air side-entry pathways. Nevertheless, both the stick-cut method and the punch-stick method resulted in devices that could maintain the liquid level within a small fluctuation range ($<$1.6 mm), so whether the hypothesis holds will not affect the applicability of our device.

In our functional testings, no microfluidic chips were connected to the bottom container. Instead, evaporation slowly decreased the liquid level in the bottom container, which acted similarly to a microfluidic chip draining liquid from the bottom container. However, it is still interesting to see how the device will behave with the real microfluidic chips. Therefore, one of the first steps for the future work is to test the devices on bottom containers connected with certain microfluidic chips, observe the liquid height changes, and measure the flow rate through the microfluidic chips. The fluctuations of the flow rates can be calculated to quantify the device behavior.

Next, the device dimensions can be further optimized to fit a proper O-ring against the top container wall instead of using glue to secure the sealing. The sealing of the connection can be tested by blocking one of the straws on the device body and pushing air through another straw into the top container and observe if air comes out around the O-ring. A tight seal is really important for the functioning of the module, so the fitting of the O-ring should be optimized.

To fully demonstrate our device's compatibility with cell related applications, microfluidic chips can be constructed to culture cells of interest that need media perfusion, and our module can be use to maintain the perfusion. Cell behavior can be monitored and compared with other perfusion methods such as using a syringe pump.

After making sure the single-device configuration works, we can test devices in other configurations and on 96 well plates to demonstrate the high-throughput feature of our design. Device bodies can be printed connected and high-efficiency methods can be developed to assemble the membranes and O-rings.

With the capabilities of the module fully demonstrated, our devices can be used to maintain flow on high-end applications, such as the popular organ-on-chip researches. Hopefully this can bring the community a simple and robust method to work with high-throughput gravity-driven flow microfluidics.

References

[1] G. M. Whitesides, "The origins and the future of microfluidics," en, *Nature*, vol. 442, no. 7101, pp. 368–373, Jul. 2006, Number: 7101 Publisher: Nature Publishing Group, ISSN: 1476-4687. DOI: 10.1038/nature05058. URL: https://www.nature.com/articles/nature05058 (visited on 04/30/2023).

[2] K. Ren, J. Zhou, and H. Wu, "Materials for Microfluidic Chip Fabrication," *Accounts of Chemical Research*, vol. 46, no. 11, pp. 2396–2406, Nov. 2013, Publisher: American Chemical Society, ISSN: 0001-4842. DOI: 10.1021/ar300314s. URL: https://doi.org/10.1021/ar300314s (visited on 04/30/2023).

[3] L. Shang, Y. Cheng, and Y. Zhao, "Emerging Droplet Microfluidics," *Chemical Reviews*, vol. 117, no. 12, pp. 7964–8040, Jun. 2017, Publisher: American Chemical Society, ISSN: 0009-2665. DOI: 10.1021/acs.chemrev.6b00848. URL: https://doi.org/10.1021/acs.chemrev.6b00848 (visited on 04/20/2023).

[4] Y. Song and D. Cheng, "Perspective for Microfluidics," en, in *Microfluidics: Fundamental, Devices and Applications*, Section: 17 _eprint: https://onlinelibrary.wiley.com/doi/pdf/10.1002/9 John Wiley & Sons, Ltd, 2018, pp. 517–540, ISBN: 978-3-527-80064-3. DOI: 10.1002/9783527800643.ch17. URL: https://onlinelibrary.wiley.com/doi/abs/10.1002/9783527800643.ch17 (visited on 04/20/2023).

[5] A.-G. Niculescu, C. Chircov, A. C. Bîrcă, and A. M. Grumezescu, "Fabrication and Applications of Microfluidic Devices: A Review," *International Journal of Molecular Sciences*, vol. 22, no. 4, p. 2011, Feb. 2021, ISSN: 1422-0067. DOI: 10.3390/ijms22042011.

URL: https://www.ncbi.nlm.nih.gov/pmc/articles/PMC7921936/ (visited on 04/20/2023).

[6] S. Battat, D. A. Weitz, and G. M Whitesides, "An outlook on microfluidics: The promise and the challenge," en, *Lab on a Chip*, vol. 22, no. 3, pp. 530–536, 2022, Publisher: Royal Society of Chemistry. DOI: 10.1039/D1LC00731A. URL: https://pubs.rsc.org/en/content/articlelanding/2022/lc/d1lc00731a (visited on 04/10/2023).

[7] D. A. Chistiakov, A. N. Orekhov, and Y. V. Bobryshev, "Effects of shear stress on endothelial cells: Go with the flow," en, *Acta Physiologica*, vol. 219, no. 2, pp. 382–408, 2017, _eprint: https://onlinelibrary.wiley.com/doi/pdf/10.1111/apha.12725, ISSN: 1748-1716. DOI: 10.1111/apha.12725. URL: https://onlinelibrary.wiley.com/doi/abs/10.1111/apha.12725 (visited on 04/16/2024).

[8] Y.-S. J. Li, J. H. Haga, and S. Chien, "Molecular basis of the effects of shear stress on vascular endothelial cells," *Journal of Biomechanics*, vol. 38, no. 10, pp. 1949–1971, Oct. 2005, ISSN: 0021-9290. DOI: 10.1016/j.jbiomech.2004.09.030. URL: https://www.sciencedirect.com/science/article/pii/S0021929004004580 (visited on 04/16/2024).

[9] V. Narayanamurthy, Z. E. Jeroish, K. S. Bhuvaneshwari, P. Bayat, R. Premkumar, F. Samsuri, and M. M. Yusoff, "Advances in passively driven microfluidics and lab-on-chip devices: A comprehensive literature review and patent analysis," en, *RSC Advances*, vol. 10, no. 20, pp. 11 652–11 680, 2020, Publisher: Royal Society of Chemistry. DOI: 10.1039/D0RA00263A. URL: https://pubs.rsc.org/en/content/articlelanding/2020/ra/d0ra00263a (visited on 03/05/2024).

[10] S.-B. Huang, S.-S. Wang, C.-H. Hsieh, Y. C. Lin, C.-S. Lai, and M.-H. Wu, "An integrated microfluidic cell culture system for high-throughput perfusion three-dimensional cell culture-based assays: Effect of cell culture model on the results of chemosensitivity assays," en, *Lab on a Chip*, vol. 13, no. 6, pp. 1133–1143, Feb. 2013, Publisher: The Royal Society of Chemistry, ISSN: 1473-0189. DOI: 10.1039/C2LC41264K. URL:

https://pubs.rsc.org/en/content/articlelanding/2013/lc/c2lc41264k (visited on 05/17/2023).

[11] J. Y. Park, M. Morgan, A. N. Sachs, J. Samorezov, R. Teller, Y. Shen, K. J. Pienta, and S. Takayama, "Single cell trapping in larger microwells capable of supporting cell spreading and proliferation," *Microfluidics and nanofluidics*, vol. 8, no. 2, pp. 263–268, Feb. 2010, ISSN: 1613-4982. DOI: 10.1007/s10404-009-0503-9. URL: https://www.ncbi.nlm.nih.gov/pmc/articles/PMC2845479/ (visited on 05/17/2023).

[12] J. R. Lake, K. C. Heyde, and W. C. Ruder, "Low-cost feedback-controlled syringe pressure pumps for microfluidics applications," en, *PLOS ONE*, vol. 12, no. 4, e0175089, Apr. 2017, Publisher: Public Library of Science, ISSN: 1932-6203. DOI: 10.1371/journal.pone.0175089. URL: https://journals.plos.org/plosone/article?id=10.1371/journal.pone.0175089 (visited on 05/03/2023).

[13] M. R. Behrens, H. C. Fuller, E. R. Swist, J. Wu, M. M. Islam, Z. Long, W. C. Ruder, and R. Steward, "Open-source, 3D-printed Peristaltic Pumps for Small Volume Point-of-Care Liquid Handling," *Scientific Reports*, vol. 10, no. 1, pp. 1–10, Jan. 2020, Publisher: Springer Nature, ISSN: 20452322. DOI: 10.1038/s41598-020-58246-6. URL: https://search.ebscohost.com/login.aspx?direct=true&db=a9h&AN=141512870&site=eds-live&scope=site (visited on 05/03/2023).

[14] X. Zhang, Z. Chen, and Y. Huang, "A valve-less microfluidic peristaltic pumping method," *Biomicrofluidics*, vol. 9, no. 1, p. 014118, Feb. 2015, ISSN: 1932-1058. DOI: 10.1063/1.4907982. URL: https://doi.org/10.1063/1.4907982 (visited on 05/03/2023).

[15] N.-T. Nguyen and T.-Q. Truong, "A fully polymeric micropump with piezoelectric actuator," en, *Sensors and Actuators B: Chemical*, vol. 97, no. 1, pp. 137–143, Jan. 2004, ISSN: 0925-4005. DOI: 10.1016/S0925-4005(03)00521-5. URL: https://www.sciencedirect.com/science/article/pii/S0925400503005215 (visited on 04/30/2023).

[16] D.-H. Wang, L.-K. Tang, Y.-H. Peng, and H.-Q. Yu, "Principle and structure of a printed circuit board process–based piezoelectric microfluidic pump integrated into printed circuit board," *Journal of Intelligent Material Systems and Structures*, vol. 30, no. 17, pp. 2595–2604, Oct. 2019, Publisher: SAGE Publications Ltd STM, ISSN: 1045-389X. DOI: 10.1177/1045389X19869519. URL: https://doi.org/10.1177/1045389X19869519 (visited on 04/30/2023).

[17] K. Junwu, Y. Zhigang, P. Taijiang, C. Guangming, and W. Boda, "Design and test of a high-performance piezoelectric micropump for drug delivery," *Sensors and Actuators A: Physical*, vol. 121, no. 1, pp. 156–161, May 2005, ISSN: 0924-4247. DOI: 10.1016/j.sna.2004.12.002. URL: https://www.sciencedirect.com/science/article/pii/S0924424704008581 (visited on 04/11/2024).

[18] A. Hatch, A. Kamholz, G. Holman, P. Yager, and K. Bohringer, "A ferrofluidic magnetic micropump," *Journal of Microelectromechanical Systems*, vol. 10, no. 2, pp. 215–221, Jun. 2001, Conference Name: Journal of Microelectromechanical Systems, ISSN: 1941-0158. DOI: 10.1109/84.925748. URL: https://ieeexplore.ieee.org/abstract/document/925748 (visited on 04/11/2024).

[19] H. Kimura, T. Yamamoto, H. Sakai, Y. Sakai, and T. Fujii, "An integrated microfluidic system for long-term perfusion culture and on-line monitoring of intestinal tissue models," en, *Lab on a Chip*, vol. 8, no. 5, pp. 741–746, Apr. 2008, Publisher: The Royal Society of Chemistry, ISSN: 1473-0189. DOI: 10.1039/B717091B. URL: https://pubs.rsc.org/en/content/articlelanding/2008/lc/b717091b (visited on 04/11/2024).

[20] J. K. Hamilton, M. T. Bryan, A. D. Gilbert, F. Y. Ogrin, and T. O. Myers, "A new class of magnetically actuated pumps and valves for microfluidic applications," en, *Scientific Reports*, vol. 8, no. 1, p. 933, Jan. 2018, Publisher: Nature Publishing Group, ISSN: 2045-2322. DOI: 10.1038/s41598-018-19506-8. URL: https://www.nature.com/articles/s41598-018-19506-8 (visited on 04/14/2024).

[21] M. A. Unger, H.-P. Chou, T. Thorsen, A. Scherer, and S. R. Quake, "Monolithic Microfabricated Valves and Pumps by Multilayer Soft Lithography," *Science*, vol. 288, no. 5463, pp. 113–116, Apr. 2000, Publisher: American Association for the Advancement of Science. DOI: 10.1126/science.288.5463.113. URL: https://www.science.org/doi/10.1126/science.288.5463.113 (visited on 04/11/2024).

[22] J. D. Zahn, A. deshmukh, A. P. Pisano, and D. Liepmann, "Continuous On-Chip Micropumping for Microneedle Enhanced Drug Delivery," en, *Biomedical Microdevices*, vol. 6, no. 3, pp. 183–190, Sep. 2004, ISSN: 1572-8781. DOI: 10.1023/B:BMMD.0000042047.83433.96. URL: https://doi.org/10.1023/B:BMMD.0000042047.83433.96 (visited on 05/24/2023).

[23] C.-H. Wang and G.-B. Lee, "Pneumatically driven peristaltic micropumps utilizing serpentine-shape channels*," en, *Journal of Micromechanics and Microengineering*, vol. 16, no. 2, p. 341, Jan. 2006, ISSN: 0960-1317. DOI: 10.1088/0960-1317/16/2/019. URL: https://dx.doi.org/10.1088/0960-1317/16/2/019 (visited on 04/11/2024).

[24] K. Schimek, M. Busek, S. Brincker, *et al.*, "Integrating biological vasculature into a multi-organ-chip microsystem," en, *Lab on a Chip*, vol. 13, no. 18, pp. 3588–3598, Aug. 2013, Publisher: The Royal Society of Chemistry, ISSN: 1473-0189. DOI: 10.1039/C3LC50217A. URL: https://pubs.rsc.org/en/content/articlelanding/2013/lc/c3lc50217a (visited on 05/24/2023).

[25] C. K. Byun, K. Abi-Samra, Y.-K. Cho, and S. Takayama, "Pumps for microfluidic cell culture: Microfluidics and Miniaturization," en, *ELECTROPHORESIS*, vol. 35, no. 2-3, pp. 245–257, Feb. 2014, ISSN: 01730835. DOI: 10.1002/elps.201300205. URL: https://onlinelibrary.wiley.com/doi/10.1002/elps.201300205 (visited on 05/08/2023).

[26] S.-A. Lee, D. Y. No, E. Kang, J. Ju, D.-S. Kim, and S.-H. Lee, "Spheroid-based three-dimensional liver-on-a-chip to investigate hepatocyte–hepatic stellate cell interactions and flow effects," en, *Lab on a Chip*, vol. 13, no. 18, pp. 3529–3537, Aug. 2013, Pub-

lisher: The Royal Society of Chemistry, ISSN: 1473-0189. DOI: 10.1039/C3LC50197C. URL: https://pubs.rsc.org/en/content/articlelanding/2013/lc/c3lc50197c (visited on 05/14/2023).

[27] K. Feng, N. Gao, W. Zhang, K. Zhou, H. Dong, P. Wang, L. Tian, G. He, and G. Li, "Creation of Nonspherical Microparticles through Osmosis-Driven Arrested Coalescence of Microfluidic Emulsions," en, *Small*, vol. 16, no. 9, p. 1 903 884, 2020, _eprint: https://onlinelibrary.wiley.com/doi/pdf/10.1002/smll.201903884, ISSN: 1613-6829. DOI: 10.1002/smll.201903884. URL: https://onlinelibrary.wiley.com/doi/abs/10.1002/smll.201903884 (visited on 05/23/2023).

[28] A. Jajack, I. Stamper, E. Gomez, M. Brothers, G. Begtrup, and J. Heikenfeld, "Continuous, quantifiable, and simple osmotic preconcentration and sensing within microfluidic devices," en, *PLOS ONE*, vol. 14, no. 1, e0210286, Jan. 2019, Publisher: Public Library of Science, ISSN: 1932-6203. DOI: 10.1371/journal.pone.0210286. URL: https://journals.plos.org/plosone/article?id=10.1371/journal.pone.0210286 (visited on 05/23/2023).

[29] S. R. Yazdi, A. Shadmani, S. C. Bürgel, P. M. Misun, A. Hierlemann, and O. Frey, "Adding the 'heart' to hanging drop networks for microphysiological multi-tissue experiments," en, *Lab on a Chip*, vol. 15, no. 21, pp. 4138–4147, Oct. 2015, Publisher: The Royal Society of Chemistry, ISSN: 1473-0189. DOI: 10.1039/C5LC01000D. URL: https://pubs.rsc.org/en/content/articlelanding/2015/lc/c5lc01000d (visited on 04/30/2023).

[30] E. Berthier and D. J. Beebe, "Flow rate analysis of a surface tension driven passive micropump," en, *Lab on a Chip*, vol. 7, no. 11, pp. 1475–1478, Oct. 2007, Publisher: The Royal Society of Chemistry, ISSN: 1473-0189. DOI: 10.1039/B707637A. URL: https://pubs.rsc.org/en/content/articlelanding/2007/lc/b707637a (visited on 05/17/2023).

[31] I. Meyvantsson, J. W. Warrick, S. Hayes, A. Skoien, and D. J. Beebe, "Automated cell culture in high density tubeless microfluidic device arrays," en, *Lab on a Chip*, vol. 8, no. 5, pp. 717–724, Apr. 2008, Publisher: The Royal Society of Chemistry, ISSN: 1473-0189. DOI: 10.1039/B715375A. URL: https://pubs.rsc.org/en/content/articlelanding/2008/lc/b715375a (visited on 05/17/2023).

[32] D. Juncker, H. Schmid, U. Drechsler, H. Wolf, M. Wolf, B. Michel, N. de Rooij, and E. Delamarche, "Autonomous Microfluidic Capillary System," *Analytical Chemistry*, vol. 74, no. 24, pp. 6139–6144, Dec. 2002, Publisher: American Chemical Society, ISSN: 0003-2700. DOI: 10.1021/ac0261449. URL: https://doi.org/10.1021/ac0261449 (visited on 04/12/2024).

[33] L. Gervais, M. Hitzbleck, and E. Delamarche, "Capillary-driven multiparametric microfluidic chips for one-step immunoassays," en, *Biosensors and Bioelectronics*, vol. 27, no. 1, pp. 64–70, Sep. 2011, ISSN: 0956-5663. DOI: 10.1016/j.bios.2011.06.016. URL: https://www.sciencedirect.com/science/article/pii/S0956566311003800 (visited on 05/23/2023).

[34] S.-J. Kim, S. Paczesny, S. Takayama, and K. Kurabayashi, "Preprogrammed capillarity to passively control system-level sequential and parallel microfluidic flows," en, *Lab on a Chip*, vol. 13, no. 11, pp. 2091–2098, May 2013, Publisher: The Royal Society of Chemistry, ISSN: 1473-0189. DOI: 10.1039/C3LC50187F. URL: https://pubs.rsc.org/en/content/articlelanding/2013/lc/c3lc50187f (visited on 05/22/2023).

[35] Y. Fuchiwaki and H. Takaoka, "UV-laser-assisted modification of poly(methyl methacrylate) and its application to capillary-driven-flow immunoassay," en, *Journal of Micromechanics and Microengineering*, vol. 25, no. 7, p. 075 008, Jun. 2015, Publisher: IOP Publishing, ISSN: 0960-1317. DOI: 10.1088/0960-1317/25/7/075008. URL: https://dx.doi.org/10.1088/0960-1317/25/7/075008 (visited on 04/12/2024).

[36] M. Komeya, K. Hayashi, H. Nakamura, *et al.*, "Pumpless microfluidic system driven by hydrostatic pressure induces and maintains mouse spermatogenesis in vitro," en, *Scientific Reports*, vol. 7, no. 1, p. 15 459, Nov. 2017, Number: 1 Publisher: Nature Publishing Group, ISSN: 2045-2322. DOI: 10.1038/s41598-017-15799-3. URL: https://www.nature.com/articles/s41598-017-15799-3 (visited on 04/30/2023).

[37] V. N. Goral, C. Zhou, F. Lai, and P. K. Yuen, "A continuous perfusion microplate for cell culture," en, *Lab on a Chip*, vol. 13, no. 6, pp. 1039–1043, Feb. 2013, Publisher: The Royal Society of Chemistry, ISSN: 1473-0189. DOI: 10.1039/C2LC41102D. URL: https://pubs.rsc.org/en/content/articlelanding/2013/lc/c2lc41102d (visited on 05/08/2023).

[38] D. W. Lee, N. Choi, and J. H. Sung, "A microfluidic chip with gravity-induced unidirectional flow for perfusion cell culture," en, *Biotechnology Progress*, vol. 35, no. 1, e2701, 2019, _eprint: https://onlinelibrary.wiley.com/doi/pdf/10.1002/btpr.2701, ISSN: 1520-6033. DOI: 10.1002/btpr.2701. URL: https://onlinelibrary.wiley.com/doi/abs/10.1002/btpr.2701 (visited on 04/30/2023).

[39] Y.-T. Kao, T. S. Kaminski, W. Postek, J. Guzowski, K. Makuch, A. Ruszczak, F. v. Stetten, R. Zengerle, and P. Garstecki, "Gravity-driven microfluidic assay for digital enumeration of bacteria and for antibiotic susceptibility testing," en, *Lab on a Chip*, vol. 20, no. 1, pp. 54–63, Dec. 2019, Publisher: The Royal Society of Chemistry, ISSN: 1473-0189. DOI: 10.1039/C9LC00684B. URL: https://pubs.rsc.org/en/content/articlelanding/2020/lc/c9lc00684b (visited on 05/05/2023).

[40] H. Yamada, Y. Yoshida, N. Terada, S. Hagihara, T. Komatsu, and A. Terasawa, "Fabrication of gravity-driven microfluidic device," *Review of Scientific Instruments*, vol. 79, no. 12, p. 124 301, Dec. 2008, ISSN: 0034-6748. DOI: 10.1063/1.3030859. URL: https://doi.org/10.1063/1.3030859 (visited on 05/05/2023).

[41] H. Gu, F. Rong, B. Tang, Y. Zhao, D. Fu, and Z. Gu, "Photonic Crystal Beads from Gravity-Driven Microfluidics," *Langmuir*, vol. 29, no. 25, pp. 7576–7582, Jun. 2013, Publisher: American Chemical Society, ISSN: 0743-7463. DOI: 10.1021/la4008069. URL: https://doi.org/10.1021/la4008069 (visited on 04/20/2023).

[42] M. Marimuthu and S. Kim, "Pumpless steady-flow microfluidic chip for cell culture," en, *Analytical Biochemistry*, vol. 437, no. 2, pp. 161–163, Jun. 2013, ISSN: 0003-2697. DOI: 10.1016/j.ab.2013.02.007. URL: https://www.sciencedirect.com/science/article/pii/S0003269713000791 (visited on 05/05/2023).

[43] L. R. Soenksen, T. Kassis, M. Noh, L. G. Griffith, and D. L. Trumper, "Closed-loop feedback control for microfluidic systems through automated capacitive fluid height sensing," en, *Lab on a Chip*, vol. 18, no. 6, pp. 902–914, Mar. 2018, Publisher: The Royal Society of Chemistry, ISSN: 1473-0189. DOI: 10.1039/C7LC01223C. URL: https://pubs.rsc.org/en/content/articlelanding/2018/lc/c7lc01223c (visited on 05/19/2023).

[44] L. J. Y. Ong, L. H. Chong, L. Jin, P. K. Singh, P. S. Lee, H. Yu, A. Ananthanarayanan, H. L. Leo, and Y.-C. Toh, "A pump-free microfluidic 3D perfusion platform for the efficient differentiation of human hepatocyte-like cells," en, *Biotechnology and Bioengineering*, vol. 114, no. 10, pp. 2360–2370, 2017, _eprint: https://onlinelibrary.wiley.com/doi/pdf/10.10 ISSN: 1097-0290. DOI: 10.1002/bit.26341. URL: https://onlinelibrary.wiley.com/doi/abs/10.1002/bit.26341 (visited on 05/05/2023).

[45] X. Zhu, L. Y. Chu, B.-h. Chueh, M. Shen, B. Hazarika, N. Phadke, and S. Takayama, "Arrays of horizontally-oriented mini-reservoirs generate steady microfluidic flows for continuous perfusion cell culture and gradient generation," en, *Analyst*, vol. 129, no. 11, pp. 1026–1031, Oct. 2004, Publisher: The Royal Society of Chemistry, ISSN: 1364-5528. DOI: 10.1039/B407623K. URL: https://pubs.rsc.org/en/content/articlelanding/2004/an/b407623k (visited on 05/05/2023).

[46] T. Kim and Y.-H. Cho, "A pumpless cell culture chip with the constant medium perfusion-rate maintained by balanced droplet dispensing," en, *Lab on a Chip*, vol. 11, no. 10, pp. 1825–1830, May 2011, Publisher: The Royal Society of Chemistry, ISSN: 1473-0189. DOI: 10.1039/C1LC20234K. URL: https://pubs.rsc.org/en/content/articlelanding/2011/lc/c1lc20234k (visited on 05/05/2023).

[47] T. Kim, I. Doh, and Y.-H. Cho, "On-chip three-dimensional tumor spheroid formation and pump-less perfusion culture using gravity-driven cell aggregation and balanced droplet dispensing," *Biomicrofluidics*, vol. 6, no. 3, p. 034 107, Jul. 2012, ISSN: 1932-1058. DOI: 10.1063/1.4739460. URL: https://doi.org/10.1063/1.4739460 (visited on 05/19/2023).

[48] G. S. Jeong, J. Oh, S. B. Kim, M. R. Dokmeci, H. Bae, S.-H. Lee, and A. Khademhosseini, "Siphon-driven microfluidic passive pump with a yarn flow resistance controller," en, *Lab on a Chip*, vol. 14, no. 21, pp. 4213–4219, Sep. 2014, Publisher: The Royal Society of Chemistry, ISSN: 1473-0189. DOI: 10.1039/C4LC00510D. URL: https://pubs.rsc.org/en/content/articlelanding/2014/lc/c4lc00510d (visited on 05/05/2023).

[49] L. Kim, Y.-C. Toh, J. Voldman, and H. Yu, "A practical guide to microfluidic perfusion culture of adherent mammalian cells," en, *Lab on a Chip*, vol. 7, no. 6, pp. 681–694, May 2007, Publisher: The Royal Society of Chemistry, ISSN: 1473-0189. DOI: 10.1039/B704602B. URL: https://pubs.rsc.org/en/content/articlelanding/2007/lc/b704602b (visited on 05/15/2024).

[50] Y.-j. J. Shuang SU, "The Research Progress of Perfusion Mammalian Cell Culture," cn, *China Biotechnology*, vol. 39, no. 3, pp. 105–110, Apr. 2019, ISSN: 1671-8135. DOI: 10.13523/j.cb.20190313. URL: https://manu60.magtech.com.cn/biotech/EN/abstract/abstract6355.shtml (visited on 05/15/2024).

[51] B. S. Cho, T. G. Schuster, X. Zhu, D. Chang, G. D. Smith, and S. Takayama, "Passively Driven Integrated Microfluidic System for Separation of Motile Sperm," *Analytical*

Chemistry, vol. 75, no. 7, pp. 1671–1675, Apr. 2003, Publisher: American Chemical Society, ISSN: 0003-2700. DOI: 10.1021/ac020579e. URL: https://doi.org/10.1021/ac020579e (visited on 05/15/2024).

[52] B. Yao, G.-a. Luo, X. Feng, W. Wang, L.-x. Chen, and Y.-m. Wang, "A microfluidic device based on gravity and electric force driving for flow cytometry and fluorescence activated cell sorting," en, *Lab on a Chip*, vol. 4, no. 6, pp. 603–607, 2004, Publisher: Royal Society of Chemistry. DOI: 10.1039/B408422E. URL: https://pubs.rsc.org/en/content/articlelanding/2004/lc/b408422e (visited on 05/15/2024).

[53] W. Gao, M. Liu, S. Chen, C. Zhang, and Y. Zhao, "Droplet microfluidics with gravity-driven overflow system," *Chemical Engineering Journal*, vol. 362, pp. 169–175, Apr. 2019, ISSN: 1385-8947. DOI: 10.1016/j.cej.2019.01.026. URL: https://www.sciencedirect.com/science/article/pii/S1385894719300324 (visited on 04/15/2024).

[54] N. Limjanthong, Y. Tohbaru, T. Okamoto, *et al.*, "Gravity-driven microfluidic device placed on a slow-tilting table enables constant unidirectional perfusion culture of human induced pluripotent stem cells," en, *Journal of Bioscience and Bioengineering*, vol. 135, no. 2, pp. 151–159, Feb. 2023, ISSN: 13891723. DOI: 10.1016/j.jbiosc.2022.11.007. URL: https://linkinghub.elsevier.com/retrieve/pii/S1389172322003462 (visited on 10/30/2023).

[55] K. Mizoue, M. H. Phan, C.-H. D. Tsai, M. Kaneko, J. Kang, and W. K. Chung, "Gravity-Based Precise Cell Manipulation System Enhanced by In-Phase Mechanism," en, *Micromachines*, vol. 7, no. 7, p. 116, Jul. 2016, Number: 7 Publisher: Multidisciplinary Digital Publishing Institute, ISSN: 2072-666X. DOI: 10.3390/mi7070116. URL: https://www.mdpi.com/2072-666X/7/7/116 (visited on 10/30/2023).

[56] X. Wang, D. Zhao, D. T. T. Phan, J. Liu, X. Chen, B. Yang, C. C. W. Hughes, W. Zhang, and A. P. Lee, "A hydrostatic pressure-driven passive micropump enhanced with siphon-based autofill function," en, *Lab on a Chip*, vol. 18, no. 15, pp. 2167–

2177, Jul. 2018, Publisher: The Royal Society of Chemistry, ISSN: 1473-0189. DOI: 10.1039/C8LC00236C. URL: https://pubs.rsc.org/en/content/articlelanding/2018/lc/c8lc00236c (visited on 01/18/2023).

[57] R. J. Roselli and K. R. Diller, "General Microscopic Approach for Biofluid Transport," en, in *Biotransport: Principles and Applications*, R. J. Roselli and K. R. Diller, Eds., New York, NY: Springer, 2011, pp. 389–485, ISBN: 978-1-4419-8119-6. DOI: 10.1007/978-1-4419-8119-6_7. URL: https://doi.org/10.1007/978-1-4419-8119-6_7 (visited on 04/23/2024).

[58] R. J. Roselli and K. R. Diller, "Macroscopic Approach for Biofluid Transport," en, in *Biotransport: Principles and Applications*, R. J. Roselli and K. R. Diller, Eds., New York, NY: Springer, 2011, pp. 169–317, ISBN: 978-1-4419-8119-6. DOI: 10.1007/978-1-4419-8119-6_5. URL: https://doi.org/10.1007/978-1-4419-8119-6_5 (visited on 04/23/2024).

[59] D. S. Lemons, T. C. Lipsombe, and R. J. Faehl, "Vertical quasistatic Poiseuille flow: Theory and experiment," *American Journal of Physics*, vol. 90, no. 1, pp. 59–63, Jan. 2022, ISSN: 0002-9505. DOI: 10.1119/10.0006245. URL: https://doi.org/10.1119/10.0006245 (visited on 04/17/2024).

[60] *Moisture Handbook*. URL: https://macinstruments.com/resources/moisture-handbook/ (visited on 04/23/2024).

[61] A. L. Buck, "New Equations for Computing Vapor Pressure and Enhancement Factor," *Journal of Applied Meteorology (1962-1982)*, vol. 20, no. 12, pp. 1527–1532, 1981, Publisher: American Meteorological Society, ISSN: 0021-8952. URL: https://www.jstor.org/stable/26180379 (visited on 04/23/2024).

[62] M. M. Shah, "Analytical formulas for calculating water evaporation from pools," English, *ASHRAE Transactions*, vol. 114, no. 2, pp. 610–619, Jul. 2008, Publisher: American Society of Heating, Refrigerating, and Air-Conditioning Engineers, Inc. (ASHRAE),

ISSN: 00012505. URL: https://go.gale.com/ps/i.do?p=AONE&sw=w&issn=00012505&v=2.1&it=r&id=GALE%7CA201378240&sid=googleScholar&linkaccess=abs (visited on 04/16/2024).

[63] M. M. Shah, "Improved method for calculating evaporation from indoor water pools," *Energy and Buildings*, vol. 49, pp. 306–309, Jun. 2012, ISSN: 0378-7788. DOI: 10.1016/j.enbuild.2012.02.026. URL: https://www.sciencedirect.com/science/article/pii/S0378778812001041 (visited on 03/05/2024).

[64] M. M. Shah, "Evaluation of Available Correlations for Rate of Evaporation from Undisturbed Water Pools to Quiet Air," *HVAC&R Research*, vol. 8, no. 1, pp. 125–131, Jan. 2002, Publisher: Taylor & Francis _eprint: https://doi.org/10.1080/10789669.2002.10391292, ISSN: 1078-9669. DOI: 10.1080/10789669.2002.10391292. URL: https://doi.org/10.1080/10789669.2002.10391292 (visited on 04/16/2024).

[65] T. Poós and E. Varju, "Mass transfer coefficient for water evaporation by theoretical and empirical correlations," *International Journal of Heat and Mass Transfer*, vol. 153, p. 119 500, Jun. 2020, ISSN: 0017-9310. DOI: 10.1016/j.ijheatmasstransfer.2020.119500. URL: https://www.sciencedirect.com/science/article/pii/S0017931019341791 (visited on 02/28/2024).

[66] E. Norman, "The Expanding World of PTFE," en, *Cellular Polymers*, vol. 6, no. 1, pp. 37–51, Jan. 1987, Publisher: SAGE Publications Ltd STM, ISSN: 0262-4893. DOI: 10.1177/026248938700600104. URL: https://doi.org/10.1177/026248938700600104 (visited on 05/03/2024).

[67] "Introduction," in *Handbook of Plastics Joining (Second Edition)*, M. J. Troughton, Ed., Boston: William Andrew Publishing, Jan. 2009, pp. xxi–xxii, ISBN: 978-0-8155-1581-4. DOI: 10.1016/B978-0-8155-1581-4.50002-0. URL: https://www.sciencedirect.com/science/article/pii/B9780815515814500020 (visited on 05/03/2024).

[68] D. M. Conning and J. Firth, "Toxicity of polypropylene in tissue culture," *Food and Cosmetics Toxicology*, vol. 7, pp. 461–472, Jan. 1969, ISSN: 0015-6264. DOI: 10.1016/S0015-6264(69)80426-8. URL: https://www.sciencedirect.com/science/article/pii/S0015626469804268 (visited on 04/24/2024).

[69] M. E. Fay, O. Oshinowo, E. Iffrig, *et al.*, "iCLOTS: Open-source, artificial intelligence-enabled software for analyses of blood cells in microfluidic and microscopy-based assays," en, *Nature Communications*, vol. 14, no. 1, p. 5022, Aug. 2023, Publisher: Nature Publishing Group, ISSN: 2041-1723. DOI: 10.1038/s41467-023-40522-4. URL: https://www.nature.com/articles/s41467-023-40522-4 (visited on 04/25/2024).